Multifunctional eugenol-enriched PEO-based electrospun and photo-crosslinked scaffolds for wound healing applications

APRIL 2026 | VOLUME 49

ELSEVIER

MATERIALS TODAY

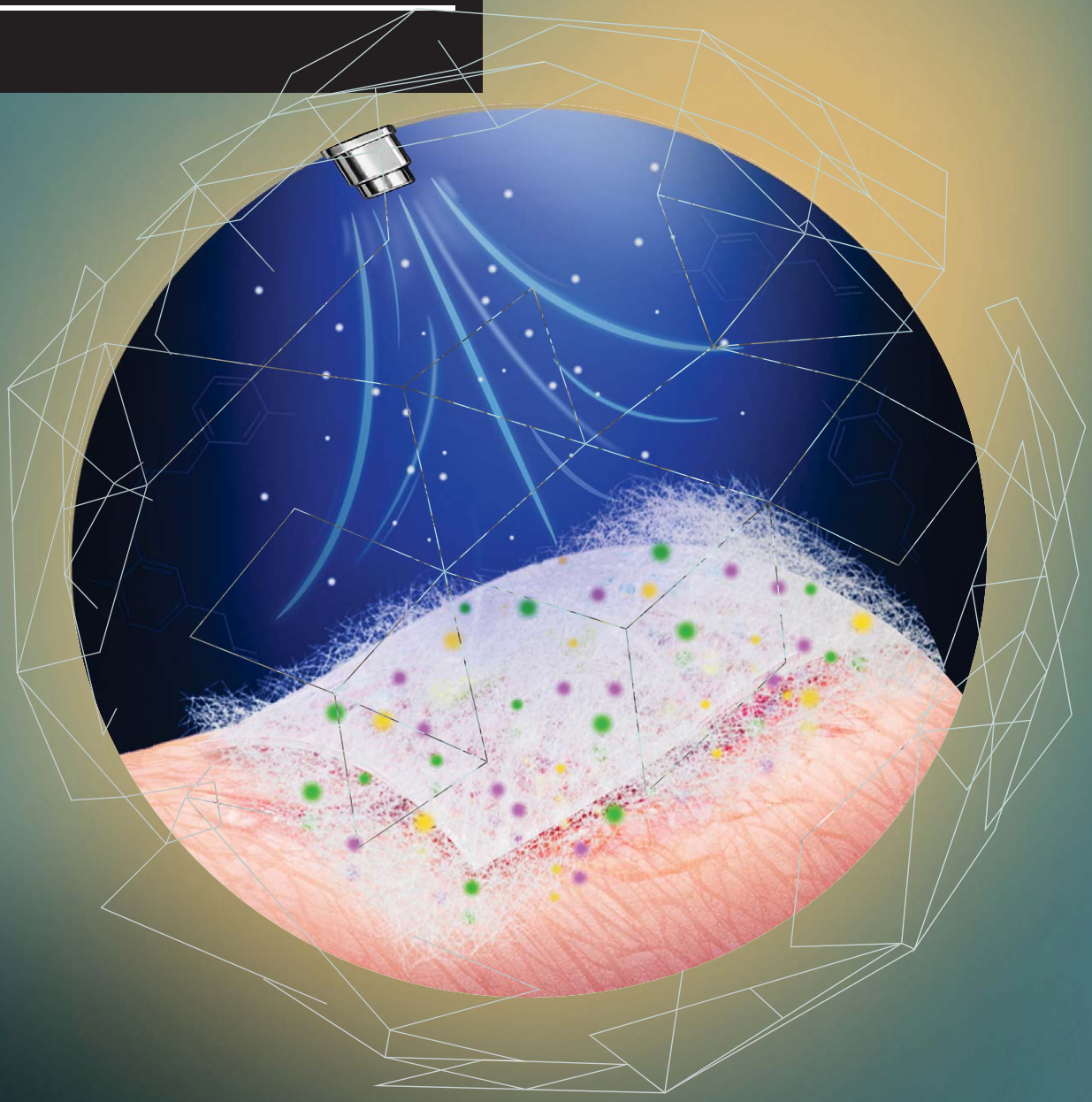

APPLIED

Applied Materials Today 49 (2026) 103136

Contents lists available at ScienceDirect

Applied Materials Today

journal homepage: www.elsevier.com/locate/apmt

Multifunctional eugenol-enriched PEO-based electrospun and photo-crosslinked scaffolds for wound healing applications

A.C. Scalia [a,†], J.A. Talamo Ruiz [b,†], S. Dalle Vacche [b], R. Bongiovanni [b], P. Lacroix-Desmazes [c], A. Cochis [a], A. Vitale [b,*]

[a] Department of Health Sciences, Center for Translational Research on Autoimmune and Allergic Diseases CAAD, Università del Piemonte Orientale (UPO), Novara 28100, Italy
[b] Department of Applied Science and Technology, Politecnico di Torino, Torino 10129, Italy
[c] ICGM, Univ Montpellier, CNRS, ENSCM, Montpellier, France

ARTICLE INFO

Keywords:
Bioactive polymers
Poly(ethylene oxide)
Nanofibrous scaffolds
Photo-crosslinked networks
Tissue regeneration

ABSTRACT

The development of multifunctional wound dressings that simultaneously prevent infection and promote tissue regeneration remains a critical challenge in regenerative medicine. In this study, electrospun poly(ethylene oxide) (PEO)-based nanofibrous membranes were functionalized with eugenol (EU) and eugenol methacrylate (EUMA) as bioactive agents. The membranes were subsequently photo-crosslinked to enhance structural stability and biomedical applicability. Different concentrations of bioactive compounds were evaluated, and the optimized formulations produced scaffolds with uniform, defect-free fibers averaging 316–340 nm in diameter. Physico-chemical characterization confirmed that the scaffolds possess mechanical robustness, flexibility, hydrophilicity, and permeability, which are key requirements for effective wound dressing performance. Both EU- and EUMA-functionalized scaffolds were cytocompatible and non-toxic. In addition, they exhibited notable antibacterial and anti-biofilm activity. Membranes containing 5% EU showed superior inhibition of Gram-positive bacterial growth, whereas those incorporating 5% EUMA provided enhanced cytoprotective and pro-regenerative effects. In vitro wound-healing assays using human mesenchymal stromal cells demonstrated that EUMA-functionalized scaffolds achieved an 85% reduction in wound width within 24 h in a 2D model. Consistently, in a 3D reconstructed human epidermis model, both EU- and EUMA-doped scaffolds accelerated wound closure by approximately twofold compared to undoped PEO. This study thus provides a previously unexplored structure-function comparison between native eugenol and its methacrylated derivative incorporated into photo-crosslinked electrospun PEO scaffolds, elucidating how chemical modification governs the balance between antimicrobial and regenerative performance. Overall, the developed PEO-based nanofibrous scaffolds offer a scalable, cost-effective, and versatile platform for next-generation smart wound dressings designed to support both infection control and tissue repair.

1. Introduction

Acute and chronic wounds constitute a major clinical and economic challenge worldwide, accounting for substantial morbidity and mortality rates, healthcare costs, and reduced quality of life for patients [1,2]. In particular, chronic wounds, which affect about 2 % of the population in developed countries, severely impact the quality of life of patients by causing pain, loss of productivity, psychological distress, and economic burden [3]. In addition to individual management and treatment costs, the global economic burden of chronic wounds is estimated to reach tens of billions of dollars annually, with the wound care market projected to grow to approximately 20 billion USD by 2027 [4].

Skin damage resulting from external mechanical forces, burns, chemical accidents, or chronic disease-related ulcers can significantly compromise both the structural and functional integrity of the skin, and in many cases, predispose the site to microbial infection. Although the body rapidly initiates a coordinated wound healing process, the injured site remains highly susceptible to bacterial and fungal colonization.

* Corresponding author.
E-mail address: alessandra.vitale@polito.it (A. Vitale).
† These authors contributed equally to the work.

https://doi.org/10.1016/j.apmt.2026.103136
Received 10 November 2025; Received in revised form 27 January 2026; Accepted 4 February 2026
Available online 10 February 2026

Colonization of the wound area typically begins with Gram-positive species, which elicit only weak immune responses, followed by Gram-negative bacteria that eventually predominate in the wound microenvironment [5]. Both groups sustain a pro-inflammatory state that disrupts key processes such as re-epithelialization and tissue regeneration. This imbalance ultimately drives the progression from an acute to a chronic wound [6–8]. Effective prevention of this progression relies on the prompt application of advanced wound dressings that not only provide a barrier against microbial invasion but also create a supportive microenvironment for cellular proliferation, angiogenesis, and tissue remodeling [9–11].

In contemporary clinical practice, wound dressings are primarily used to protect injured tissue from microbial invasion and to support healing by maintaining a moist environment conducive to re-epithelialization. Traditional dressings, such as cotton, gauze, and bandages, are widely employed due to their low cost and absorbency; however, their role is largely passive. These materials may cause wound dehydration, adhere to the tissue surface, and lead to secondary injury upon removal, thereby delaying healing [12,13]. In contrast, next-generation wound dressings increasingly adopt multifunctional and synergistic therapeutic approaches that extend beyond superficial protection. Effective wound management, particularly for complex or chronic wounds, requires systems capable of promoting both epidermal and dermal regeneration, while also supporting the repair and remodeling of deeper tissue layers. This comprehensive regenerative capacity is essential to restore full tissue functionality, prevent fibrosis, and reduce the risk of wound recurrence [14]. Recent progress in tissue engineering and biomaterials has therefore focused on multifunctional scaffolds capable of interacting with different cell types, modulating inflammatory responses, and promoting regeneration in both superficial and deep tissues through coordinated therapeutic mechanisms. Within this framework, active healing strategies based on biofunctional scaffolds that deliver therapeutic cues in a controlled and localized manner have emerged as a key trend in advanced wound care [15–17]. These approaches rely on multifunctional synergistic therapy, in which antimicrobial, anti-inflammatory, antioxidant, and pro-regenerative functions are integrated within a single dressing to effectively address the complex and dynamic wound microenvironment.

Various advanced materials [10,18], including films [19,20], foams [21,22], sponges [23,24], hydrogels [25,26], and nanofiber membranes, have been explored for these purposes. Electrospinning is a fiber fabrication technique in which a high-voltage electric field is applied to a polymer solution or melt, generating a charged jet that undergoes elongation and solvent evaporation, ultimately producing continuous fibers with micro- to nanoscale diameters [27,28]. Owing to its simplicity, scalability, and ability to generate fibrous architectures that closely mimic the native extracellular matrix, electrospinning has emerged as one of the most widely investigated techniques for the fabrication of advanced wound dressings [29–31]. The high surface-to-volume ratio, interconnected porosity, and tunable fiber morphology of electrospun scaffolds promote cell adhesion, proliferation, and migration, while enabling efficient gas exchange and moisture regulation at the wound site. Moreover, electrospinning enables the incorporation and controlled release of bioactive agents, supporting integrated healing strategies that modulate inflammation, prevent infection, and stimulate tissue regeneration [32–34]. A wide range of polymers has been processed by electrospinning for wound healing applications, encompassing synthetic polymers such as poly(ethylene oxide) (PEO), poly(ε-caprolactone), poly(lactic acid), poly (lactic-co-glycolic acid), and polyurethane, as well as natural polymers including collagen, gelatin, chitosan, alginate, silk fibroin, and hyaluronic acid [35–37]. While synthetic polymers offer mechanical strength and processability, they often lack cell-binding sites and biodegradability, limiting their regenerative potential. Natural polymers, on the other hand, combine biocompatibility, low cytotoxicity, and intrinsic bioactivity that can accelerate tissue repair [38,39], but they typically exhibit limited mechanical stability. To address these limitations, recent research has increasingly focused on polymer blending, surface functionalization, and post-processing strategies, such as chemical or photo-induced crosslinking, to tailor scaffold stability and biological performance [40,41]. Within this framework, PEO represents an attractive platform due to its biocompatibility, chemical inertness, excellent thermal properties, and ease of electrospinning, making it well suited for biomedical applications. When combined with bioactive compounds and appropriate network stabilization strategies, PEO-based electrospun scaffolds can be transformed from passive matrices into active wound dressings capable of supporting infection control and tissue regeneration.

Although electrospun mats are promising for wound healing applications, their use is often limited by their inferior mechanical properties and stability [39]. A widely used strategy to overcome these drawbacks is chemical crosslinking, which enhances the structural integrity, insolubility, and mechanical robustness of the fibers, while also improving their functional performance [42]. In particular, PEO-based electrospun materials can be crosslinked through a photo-induced process using a suitable photoinitiator and crosslinker. This approach forms a covalent network that preserves the beneficial properties of PEO while imparting superior stability and functionality [43–46].

Among the natural compounds explored for wound dressing development, eugenol stands out for its broad bioactivity. Eugenol (4-allyl-2-methoxyphenol, EU) is a natural phenolic compound, primarily derived from clove but also present in nutmeg, cinnamon, turmeric, basil, rosemary, and other aromatic plants [47–50]. EU exhibits strong antimicrobial and antioxidant activities, alongside additional antiviral, anti-inflammatory, anesthetic, anticarcinogenic, and neuroprotective effects, making it valuable across food, cosmetic, agricultural, and especially pharmaceutical applications [51–55]. Notably, in the context of increasing antibiotic resistance, EU has shown broad-spectrum efficacy against Gram-positive bacteria (e.g., *Staphylococcus epidermidis, Listeria monocytogenes, Bacillus subtilis, Streptococcus pneumoniae*) [56,57], Gram-negative bacteria (e.g., *Escherichia coli, Salmonella spp.*, *Pseudomonas aeruginosa*) [58,59], and fungi such as *Penicillium spp* [60,61]. The antibacterial activity of EU is primarily attributed to its chemical structure and its multifaceted interactions with bacterial cells. These include disruption of cell wall and membrane integrity, inhibition of biofilm formation and DNA synthesis, induction of oxidative stress–mediated apoptosis, scavenging of reactive oxygen and nitrogen species, and interference with microbial proteins and nucleic acids, ultimately leading to cell lysis [62]. Moreover, EU serves as a valuable precursor for chemical modification, as it contains both hydroxyl and allylic functional groups. For instance, its methacrylate derivatives [63] offer functional groups suitable for photoinduced processes while potentially improving the bioactivity of EU [64–66].

Despite the extensive investigation of electrospun wound dressings and the well-established bioactivity of eugenol, the incorporation of eugenol and its methacrylate derivative into photo-crosslinked PEO electrospun scaffolds remains largely unexplored. In particular, the combined role of photo-induced network formation and essential oil-derived functionalization in governing antibacterial, antibiofilm, cytocompatible, and pro-regenerative responses has not been systematically addressed. The novelty of this work lies in the development of stable, multifunctional electrospun PEO scaffolds functionalized with eugenol-based compounds via photo-crosslinking, enabling a direct structure-function comparison between native eugenol and its methacrylated derivative within a photo-crosslinked fibrous network.

In this context, the present study reports the fabrication of biocompatible and antibacterial fibrous scaffolds through electrospinning followed by photo-induced crosslinking. PEO-based mats were functionalized with EU or its methacrylate derivative (EUMA) at different concentrations (0–5 wt %). The resulting scaffolds were thoroughly characterized to assess crosslinking efficiency and their chemical, physical, and mechanical properties, including morphology, solvent

resistance, permeability, and tensile strength. Biological performance was evaluated through direct and indirect cytocompatibility assays, as well as antibacterial activity against *Staphylococcus epidermidis* (Gram-positive) and *E. coli*(Gram-negative), antibiofilm efficacy, and cell–bacteria co-culture studies. Finally, the pro-regenerative potential of the scaffolds was examined both in monolayer cultures of deep-layer cells and in a 3D model using a commercial Reconstructed Human Epidermis.

2. Materials and methods

2.1. Materials

High molecular weight polyethylene oxide (PEO, MW 1000,000 g/mol), benzophenone (≥99 %), trimethylolpropane triacrylate (TMPTA), eugenol (EU, 99 %) and ethanol were purchased from Sigma Aldrich. Ethoxy eugenyl methacrylate (EUMA) was synthesized following the two-step procedure described in a previous work [63]. All other chemicals were obtained from Sigma-Aldrich. The chemical structures of the compounds used in the fabrication of the electrospun mats are provided in the Supporting Information (Figure S1).

2.2. Electrospun mats preparation

5 wt. % PEO solutions were prepared using a water/ethanol weight ratio of 1/1 as solvent. The solutions were homogenized overnight by magnet stirring at room temperature. TMPTA was added obtaining a 3:1 PEO:TMPTA weight ratio. Then, 2 wt. % (with respect to PEO) of benzophenone and the desired amount of antibacterial agent (i.e., EU or EUMA) were included. The mixture was stirred for 10 min. Different solutions with different amounts of antibacterial agent were prepared, namely 1, 3 and 5 wt. % with respect to PEO. Table 1 summarizes the composition and the names associated with the different samples.

Electrospinning was performed by an E-fiber electrospinning system SKE apparatus in horizontal setup with high-voltage power supply, a programmable syringe pump, and a stationary collector. Aluminum foils were used as the substrate during electrospinning. The syringe tip diameter was 1 mm; the working distance between the needle and the collector was set as 20 cm; a flow rate of 0.3 ml/h and a voltage between 10 and 14 kV was applied. The electrospun mats were prepared at ambient conditions: temperature of 20–23 °C and relative humidity of 45–50 %.

After electrospinning, the fibrous mats were carefully peeled off from the aluminum substrate to obtain free-standing scaffolds. Samples with a thickness of around 50–100 μm were fabricated. The thickness was measured by digital micrometer; for each sample at least 5 values in different spots were collected and the average value was calculated.

Photo-crosslinking was performed by a high-pressure mercury-xenon lamp equipped with an optical fiber (LIGHTNINGCURE Spot light source LC8, Hamamatsu). The irradiation had an intensity of 90 mW/cm^2 on the surface of the specimens, and was performed for 10 min in inert atmosphere by purging nitrogen gas. The UV light intensity was measured by a UV Power Puck II (EIT Instrument Markets).

Table 1
Composition and name details of the scaffolds fabricated.

Sample name	Additive	
	Type	Concentration (wt %)
PEO	-	-
PEO-1EU	Eugenol	1
PEO-3EU	Eugenol	3
PEO-5EU	Eugenol	5
PEO-1EUMA	Eugenol methacrylate	1
PEO-3EUMA	Eugenol methacrylate	3
PEO-5EUMA	Eugenol methacrylate	5

2.3. Electrospun mats characterization

For assessing the chemical bonds and compositions of electrospun fibers prior and after UV curing, attenuated total reflection FTIR spectroscopy (ATR-FTIR, Thermo Fisher Scientific Nicolet iS50) was used. Conversion was calculated by monitoring the decrease in the area A of the ATR-FTIR absorption band of the reactive functionality (acrylate C=C peak around 1638 cm^{-1}) with time *t*. The area was normalized by a constant signal in the spectra (C=O peak at 1730 cm^{-1}). Percent C=C conversion is given by Eq. (1):

$$Conversion\ (\%) = \left(1 - \frac{|A_{C=C}/A_{C=O}|_t}{|A_{C=C}/A_{C=O}|_{t=0}}\right) \times 100 \quad (1)$$

Three repetitions were performed, and the average conversion value and the standard deviation were calculated.

The electrospun scaffold morphology was characterized by FE-SEM (Field Emission Scanning Electron Microscopy, ZEISS Supra 40). The samples were coated with a thin Pt film via sputtering (by a Quorum Q150T ES sputter coater) prior to analysis. Fiber diameter and surface porosity were quantified by analyzing FE-SEM micrographs using ImageJ software. For each sample, approximately 100 fiber diameter measurements were collected. Surface porosity was determined by converting the images to 8-bit grayscale followed by binarization using the thresholding function in ImageJ. This procedure enabled segmentation of pore regions from the fibrous matrix. The threshold level was manually optimized to capture the maximum observable porosity and was kept constant across all samples to ensure consistency. The resulting binary images were subsequently analyzed to calculate the pore area fraction.

The insoluble fraction of crosslinked electrospun mats was measured by soaking the samples in a water/ethanol solution (1/1 wt ratio) for 24 h, drying them at room temperature for 48 h and calculating the mass loss of the samples. Long-term stability was evaluated using a similar procedure. The electrospun mats were immersed for one week in an aqueous solution simulating physiological conditions (glucose concentration: 5 mM; pH ≈ 7) and maintained at 37 °C. Following incubation, the samples were dried at room temperature for 48 h, and the mass loss was determined.

The mechanical properties of the samples were analyzed using the electromechanical universal testing machine INSTRON 3366 Series dual column tabletop system (ITW Test and Measurement Italia, Instron CEAST Division) equipped with a 10 kN load cell. The fibrous mats were cut to obtain samples with dimensions of 25 mm in length and 12 mm in width and placed between the clamps. A constant stretching speed of 5 mm/min at room temperature was applied, and at least three replicates were tested for each sample. During the tensile testing, stress (through machine-recorded force) and strain (the displacement based on initial cross-section area and gauge length) were measured. The Young's modulus *E* was calculated based on the initial linear elasticity regime of stress–strain curves, and the strain at break ε was recorded.

The permeability of samples was evaluated by the Elcometer 5100/1 Payne Permeability Cup in accordance with the ASTM E96 standard [67]. The cell was filled with 10 g of distilled water, and the water vapor transmission rate (WVTR) of the scaffold was determined by periodically weighing the assembly until linear.

Static contact angle measurements were performed with a FTA 1000C instrument, equipped with a video camera and image analyzer, at room temperature with the sessile drop technique. Three to five measurements were performed on each sample and the values averaged. The probe liquid was water (HPLC grade).

2.4. Biological evaluation of the electrospun mats

2.4.1. Cells cultivation

Primary human gingival fibroblasts (HGFs, ATCC CRL-2014) and

human bone marrow-derived mesenchymal stromal cells (hBMSCs, ATCC PCS-500–012) were purchased from the American Type Culture Collection. Cells were cultured in alpha-modified Eagle's medium (α-MEM, Merck, Milan, Italy) and low-glucose Dulbecco's modified Eagle's medium (DMEM-LG), supplemented with 10 % or 15 % heat-inactivated fetal bovine serum (FBS), respectively, and 1 % antibiotics (penicillin/streptomycin, Merck), at 37 °C in a humidified atmosphere with 5 % CO_2. Cells were grown until reaching 70–80 % confluence, then detached using a 0.25 % trypsin-EDTA solution (Merck), harvested, and used for experiments. For the 3D evaluation of efficacy, a commercial reconstructed human epidermis (RHE) model was used. Briefly, the model was removed from the transport gel and transferred to a 6-well plate containing 3 mL of maintenance medium.

2.4.2. Direct cytocompatibility

To investigate the possible cytotoxic effect of the nanofibrous mats, primary HGFs were put in direct contact with them. Samples were sterilized under UV-C light (30 min on each side) and then transferred in a 24 multi-well plate. A drop containing 1×10^4 cells was spotted on each sample and the plate was left in the incubator (37 °C, 5 % CO_2) for 4 h allowing cells' adhesion and spread. The samples were then submerged in a complete cell culture medium (α-MEM+10 %FBS) and left in an incubator for 24 and 48 h. After each time point, the cells' metabolic activity was analyzed using the Alamar blue assay, following the manufacturer's instructions. Briefly, the culture medium was replaced with the Alamar blue solution (0.015 % in fresh medium). Plates were then incubated in the dark for 4 h at 37 °C. After incubation, 100 μL were transferred to a new black 96-well plate, and fluorescence signals were measured using a spectrophotometer (Spark, Tecan Trading AG, Basel, CH) with an excitation wavelength of 530 nm and emission reading at 590 nm. Cells cultured in the eugenol-free medium served as a control. The experiment was conducted with three replicates for each application. Subsequently, cell morphology was examined by scanning electron microscope. Briefly, in the last time point, cells were fixed overnight at 4 °C with 2,5 % Glutaraldehyde (in PBS). Later on, samples were dehydrated with an ethanolic scale (70, 90, 100 % 1 h each) and fast-dried with the low-tension chemical compound Hexamethyldisilazane (Electronic grade, 99+ %, ThermoFisher, Waltham, USA). Samples were then covered with a nanometric gold layer (10 nm, Sputter coater, Jeol, Akishima, Japan) and observed in the SEM (JSM-IT500 InTouchScope™ Scanning Electron Microscope, Jeol).

2.4.3. Indirect cytocompatibility test

To evaluate the possible cytotoxic effect of active agents or degradation products leached from the electrospun patches, an indirect cytotoxicity test was done following the ISO 10,993 part 5 and 12 guidelines. Briefly, the samples were immersed in an appropriate volume of FBS-free cell culture medium and left in the agitator at 37 °C for 7 days. Subsequently, the conditioned medium was collected, supplemented with 10 % FBS, and used for the test. 1×10^4 cells were seeded within a 24-well sterile plate. After 24 h, necessary for proper adhesion and spreading, the culture medium was removed and replaced with the conditioned medium. Cells' metabolic activity was then analyzed through Alamar blue assay following the procedure described in paragraph 1.1. Afterward, cell morphology was evaluated using immunofluorescence. Briefly, the cells were fixed overnight with a 4 % paraformaldehyde (in PBS) at 4 °C. A solution containing phalloidin (1:500) and 4′,6-diamide-2-phenyl (DAPI, 1:1000), diluted in PBS+1 % bovine serum albumin was put in contact with cells for 1 h at room temperature, in the dark, and then the cells were observed with the EVOS FLoid Imaging System (ThermoFisher).

2.4.4. Bacterial growth condition

S. epidermidis (ATCC 51,625, Gram-positive) and *E. coli*(ATCC BAA-1161, Gram-negative) have been used to evaluate the antibacterial properties of the eugenol-doped patches. Strains were firstly streaked in the Luria-Bertani semi-solid medium (LB agar, Merck, Darmstadt, Germany) until single colonies appeared. Then, 2–3 colonies were collected, dispersed in 20 ml of LB broth, and left overnight at 37 °C in agitation (120 rpm). Before performing the tests, bacterial concentration was verified using a spectrophotometer using a 600 nm wavelength (Nanophotometer NP80, Implen, Munich, Germany). The bacterial number was then adjusted to 0.00001, corresponding to 10^3 bacteria.

2.4.5. Direct antibacterial evaluation

Before testing, samples were exposed to UV-C light (30 min on each side) and transferred to a sterile 24-multiwell plate. Tests were performed by using a slightly modified version of the ISO 22,196 procedure. Briefly, 50 μl of LB broth containing a defined number of bacteria (10^3 bacteria/sample) were placed on top of the specimens, and the plate was incubated at 37 °C for 24 h. Later on, the bacteria's viability was evaluated through metabolic activity by using the Alamar blue assay. Briefly, a solution of Alamar blue (0.0015 % in PBS) was put in contact with the infected materials and kept at 37 °C for 3 h. After that, an aliquot was transferred in a black 96-well plate, and fluorescent signals were read using the TECAN Spark Spectrophotometer (530 nm excitation and 590 nm emission). Results were normalized using the undoped material as a control. The number of viable bacteria was finally quantified using the colony-forming unit test (CFU). To detach bacteria from the membranes, specimens were transferred into sterile 2 ml tubes containing 1 ml of sterile PBS. The tubes were then immersed in an ultrasonic bath and exposed to sonic waves for 3 cycles (27 % amplitude, 5 min each). These cycles were interspersed with 3 cycles of vortex. The bacterial suspension was finally diluted in 6 serial dilutions and each of the dilutions was spotted in a slice of a semi-solid LB media. The number of bacteria was calculated using Equation (2):

$$CFU\ (mL) = (number\ of\ colonies \times dilution\ factor) \times 10^{serial\ dilution} \quad (2)$$

2.4.6. Indirect antibacterial evaluation

To evaluate the effect of the released soluble species on bacterial viability, an indirect antibacterial evaluation was performed following the ISO 10,993 part 5 and 12 guidelines, previously detailed. Briefly, the samples were immersed in an appropriate volume of LB broth and left in the agitator at 37 °C for 7 days. Subsequently, the conditioned medium was collected and used for the test. Both bacterial strains, whose number was adjusted to 10^3 bacteria/ml, were diluted in the conditioned medium and maintained for 24 h. Bacterial viability and number have been assessed with Alamar blue and CFU assay respectively, as previously described. Bacterial morphology and area coverage were examined using SEM. To estimate the area percentage covered by bacteria, the pictures obtained through SEM have been analyzed using ImageJ software.

2.4.7. Cells/bacteria co-culture

To evaluate the protective effect of the eugenol-doped patches on cells against pathogenic bacteria, an advanced cells/bacteria co-culture system has been used. A bacterial suspension, previously grown in LB broth, was diluted (1:10 ratio) in antibiotic-free α-MEM and placed at 37 °C overnight in agitation (120 RPM). Simultaneously, a defined number of HGFs (10×10^4), resuspended in complete antibiotic-free α-MEM, was seeded on top of sterile specimens, further maintained at 37 °C for 24 h. Later on, the number of bacteria was adjusted to 10^3 and placed in contact with the cell-seeded patches for 24 h. Finally, the number of cells and bacteria was counted with trypan blue and CFU, respectively. Cells' infected morphology was observed by using SEM.

2.4.8. 2D Scratch test

To evaluate the pro-regenerative potentialities of the eugenol-based active agent contained in the patches, the samples were immersed in an FBS-free cell culture medium for 7 days at 37 °C with shaking at 120 rpm, following the ISO 10,993–5 guidelines previously detailed, and

a scratch test was done. Briefly, hBMSCs were seeded into a 24-well plate at the density of 2 × 10^4 cells/well to ensure total area coverage. After 24 h, necessary for proper cell adhesion, the culture medium was removed, and a scratch was made using a 200 μl tip with gentle pressure. After scratching, the well was rinsed to remove detached cells and the conditioned medium, supplemented with 10 % of FBS was added. The plate was placed in the BioTeK CYTATION 5 imaging reader (AHSI S.p.a, Bernareggio, Italy) and photos were acquired every hour for 24 h.

2.4.9. 3D wound assay

A three-dimensional wound assay was performed using a commercial Reconstructed Human Epidermis (SkinEthic™ RHE, EPISKIN, Lyon, France) to validate the results obtained from the scratch test in monolayer. This in vitro model is composed of normal human keratinocytes cultured on an inert polycarbonate filter at the air-liquid interface. The wound was created with a scalpel, and patches were placed on top of the model. The models were then maintained in a maintenance medium (Episkin, Lyon, France) and observed at 0, 24, and 48 h. Images were captured using an optical microscope with a 20x magnification lens, and wound closure was quantified using ImageJ software.

2.4.10. Statistical analysis of data

All biological experiments were conducted in triplicate. Data analysis was performed using SPSS software (v.29.0.2.0, IBM, USA). Normality of the data and homogeneity of variances were first evaluated using the Shapiro–Wilk and Levene tests, respectively. Subsequently, differences between treated groups and controls were assessed by one-way ANOVA, followed by Tukey's post hoc test. A p-value < 0.05 was considered statistically significant.

3. Results and discussion

3.1. Scaffolds preparation by electrospinning and photo-crosslinking

Fibrous mats were fabricated via the electrospinning of PEO containing an acrylic crosslinker (i.e., TMPTA) and an antibacterial agent (either eugenol EU or eugenol methacrylate EUMA) at different concentrations, as detailed in Table 1. Subsequently, the fibrous mats were irradiated to promote radical curing, exploiting both the high reactivity of the acrylic groups in the multifunctional crosslinker and the photo-induced hydrogen abstraction from PEO. Previous studies have demonstrated that crosslinking of electrospun PEO mats enhances the stability of the nanofibrous structure [44,45]. Furthermore, the eugenol-based active agents contain C=C reactive double bonds (one allyl group per molecule in EU and both an allyl and a methacrylate group in EUMA) enabling their participation in the crosslinking process.

The chemical structure of the electrospun scaffolds before and after photocuring was characterized by ATR-FTIR spectroscopy (Fig. 1). Representative spectra are shown in Figure S2 of the Supporting Information, along with those of pure EU and EUMA for reference. As an example, Fig. 1a displays the FTIR spectra of the PEO-5EUMA sample before and after irradiation. Prior to irradiation, five characteristic peaks were detected: 1100 cm^{-1} (ether groups of PEO), 1514 cm^{-1} (C–H stretching of the aromatic ring in eugenol), 1638 cm^{-1} (C=C stretching of acrylic and vinyl groups in TMPTA, eugenol and eugenol methacrylate), 995 cm^{-1} (out-of-plane =*C*–H bending), and 1730 cm^{-1} (C=O stretching of TMPTA and EUMA). Comparable spectral features were observed for the other samples, confirming the successful incorporation of the eugenol-based active agents into the electrospun scaffolds.

Upon irradiation, a significant reduction in the intensity of the peaks at 1638 cm^{-1} and 995 cm^{-1} was observed (Fig. 1a), indicating the occurrence of the crosslinking reaction. Notably, the reduction in the absorption associated with the C=C bonds was incomplete, suggesting partial conversion. This is likely due to the limited mobility and accessibility of some reactive groups located within the polymer fiber

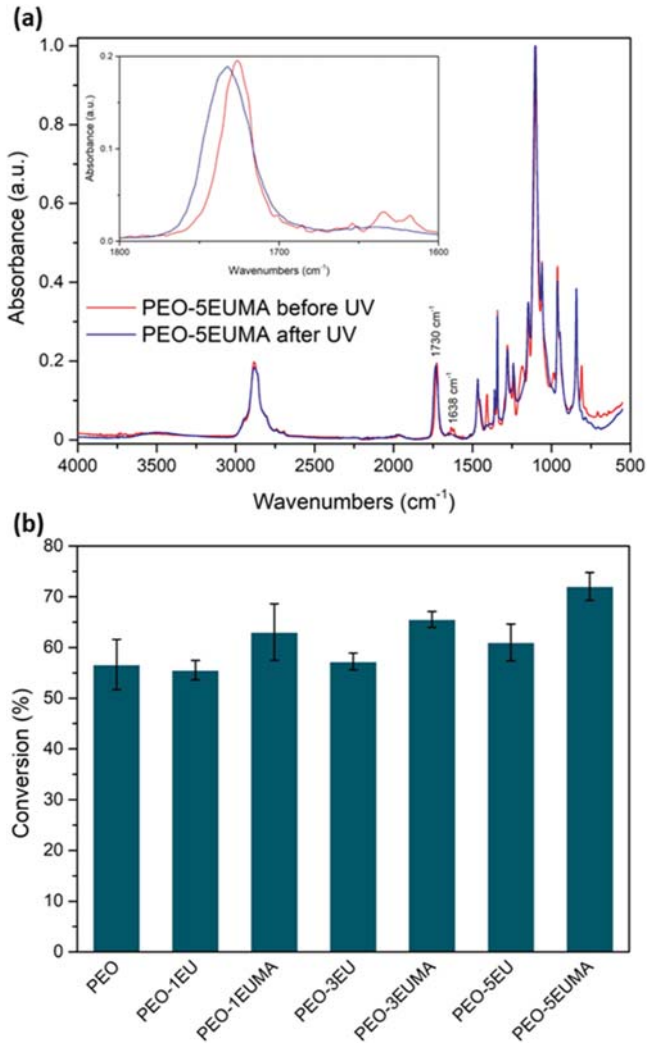

Fig. 1. Conversion analysis by ATR-FTIR spectroscopy. a) Spectra of PEO-5EUMA electrospun fibrous scaffold prior and after irradiation. The inset represents a detail of the spectra in the range 1600–1800 cm^{-1}, showing the reduction in the peak due to C=C double bonds after irradiation. b) Conversion data for the electrospun fibrous scaffolds.

structure, which may hinder their participation in the crosslinking reaction [44].

The degree of conversion was quantitatively assessed by analyzing the absorption band of the reactive C=C double bonds at approximately 1638 cm^{-1}, normalized to the carbonyl signal at 1730 cm^{-1}, and the results are reported in Fig. 1b. The conversion values ranged from medium to high (56–72 %). Across all compositions, the scaffolds containing eugenol methacrylate exhibited higher conversion rates than those containing eugenol at the same concentration. This is attributed to the bifunctional nature of EUMA, which facilitates a greater extent of crosslinking, as well as the radical inhibitor effect of the phenol in EU [68]. For both types of active agents, increasing their concentration led to a slight increase in conversion. Although the addition of EU and EUMA reduces the average functionality of the system, chain growth and crosslinking are promoted. This behavior likely reflects differences in molecular mobility: the trifunctional crosslinker contains closely spaced reactive groups that become less accessible once incorporated into the network, whereas the mono- and bifunctional eugenol derivatives remain more mobile and can more readily react with unconverted crosslinker sites, facilitating further network formation.

3.2. Chemical-physical and mechanical characterization of the nanofibrous scaffolds

The morphology of the photo-crosslinked fiber mats was investigated by FE-SEM. As shown in Fig. 2, the incorporation of both active agents did not adversely affect fiber formation during electrospinning. Uniform and defect-free fibrous scaffolds composed of straight fibers with circular cross-sections were obtained from all formulations. The addition of the active agents led to a reduction in the average fiber diameter, decreasing from 515 nm in the pure PEO sample to 289–340 nm in the doped scaffolds (Fig. 2a). This decrease is attributed to the presence of the polar additive, which enhances the stretching of the jet during electrospinning and induces the formation of ultrafine fibers that connect the primary electrospun fibers, which is a phenomenon known as electro-netting [69]. As also evident from Fig. 2a, increasing the concentration of the active agents leads to a progressive broadening of the fiber diameter distribution, indicating reduced morphological homogeneity. While the pure PEO scaffold exhibits a relatively narrow diameter distribution, samples containing 1 % and 5 % of EU or EUMA display a wider range of fiber sizes. In addition, the neat PEO scaffold shows a surface porosity of approximately 7 %, whereas both EU- and EUMA-functionalized scaffolds exhibit higher and comparable surface porosity values, averaging around 14 %. This increase in surface porosity is consistent with the observed reduction in fiber diameter and

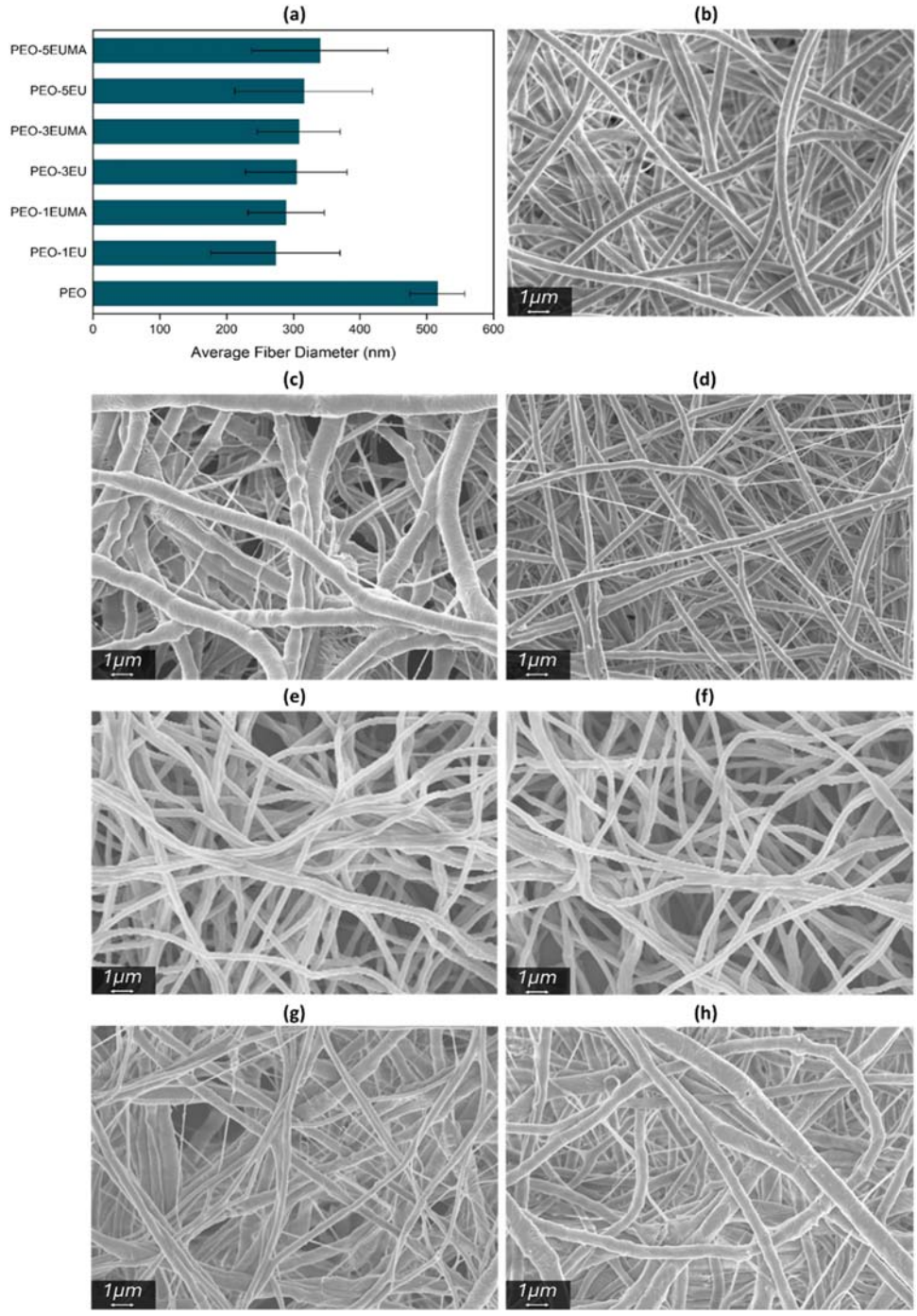

Fig. 2. Morphology of the photo-cured electrospun fibrous mats. a) Average fiber diameter. b-f) FE-SEM images of the PEO (b), PEO-1EU (c), PEO-1EUMA (d), PEO-3EU (e), PEO-3EUMA (f), PEO-5EU (g) and PEO-5EUMA (h) fibrous scaffolds.

may be advantageous for wound healing applications by facilitating gas exchange and maintaining appropriate fluid balance at the wound interface.

The solvent resistance of the crosslinked fibrous scaffolds was evaluated by insoluble fraction measurements and in terms of shape-stability.

Fig. 3a presents the values of the insoluble fraction, determined using a water/ethanol mixture as the solvent. Overall, the doped scaffolds exhibited higher insoluble fractions compared to the pure PEO sample, and this insolubility increased with the amount of antibacterial agent incorporated into the mats. This trend is consistent with the higher conversion values previously discussed (Fig. 1).

When comparing scaffolds containing different active agents (i.e., EU vs. EUMA) at the same concentration, it is evident from Fig. 3a that the eugenol-containing scaffolds consistently exhibited higher insoluble fractions. Notably, the PEO-5EU sample demonstrated the greatest solvent resistance. Although this behavior appears to contradict the conversion data, where EUMA showed a higher degree of conversion, it can be rationalized by considering the polymerization behavior of the active agents. EUMA, which contains both allyl and methacrylate groups, is more susceptible than EU (bearing only an allyl group) to termination by disproportionation. This process favors the formation of short polymer chains or microgels during irradiation, which remain soluble rather than contributing to network formation.

The insoluble fraction data also support the interpretation that the relatively moderate conversion values are due to the branched structure of the trifunctional crosslinker TMPTA. In fact, certain acrylic groups may remain unreacted due to steric hindrance or limited mobility, while a sufficient number still participate in the reaction to form an effective and insoluble crosslinked network.

The solvent resistance of the electrospun scaffolds was also evaluated by examining the preservation of their fibrous morphology after immersion in a water/ethanol solution. Fig. 3b and 3c present microscopy images of the PEO-5EU and PEO-5EUMA samples, respectively, following solvent exposure. Upon immersion, structural changes occur: the fibers become less linear, exhibit a broader size distribution, and form a more entangled network. Additionally, the fibers swell, losing their original circular cross-section. The average fiber diameters after treatment are 343.8 ± 168.4 nm for PEO-5EU and 382.2 ± 195.6 nm for PEO-5EUMA, corresponding to increases of approximately 28 nm and 42 nm, respectively, compared to the as-prepared samples. Despite these changes, the scaffolds maintain a reasonably stable morphology, indicating effective light-induced crosslinking and demonstrating promising potential for wound healing applications.

Finally, the long-term stability of the membranes was evaluated by measuring weight loss after one week of incubation under physiological conditions. All samples exhibited good stability over time. Notably, EU-doped scaffolds showed slightly higher resistance to degradation, with a weight loss of approximately 19 % for PEO-5EU, compared to 25 % for the PEO-5EUMA sample.

The mechanical properties of the fibrous scaffolds were assessed through tensile testing. Table 2 summarizes the elastic modulus (E) and the percent elongation at break (strain at break, ε) of the samples. The average values of E range from 15 to 28 MPa, which is consistent with those reported in the literature for similar PEO-based nanofibrous systems [44,70]. All the samples exhibited comparable mechanical behavior; however, a slight increase in E was observed with higher degrees of conversion, and thus with greater amounts of active agent. In contrast, the elongation at break remained relatively consistent across all samples.

As a preliminary assessment of the potential of eugenol-containing scaffolds for wound healing applications, their permeability and water wettability were also investigated. The water vapor transmission rate (WVTR) values and water contact angles are reported in Table 2. The scaffolds exhibited permeability in the range of 892–1025 g/m^2/24 h, which is consistent with previously reported data [44]. They also

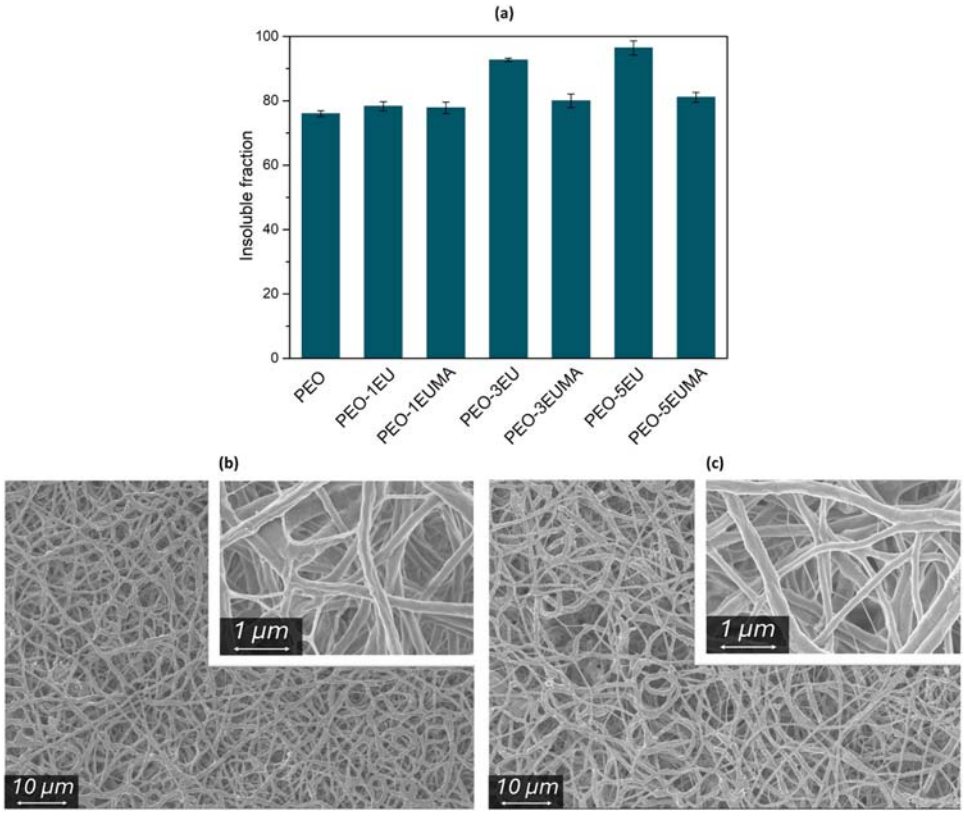

Fig. 3. Solvent resistance of the photo-cured electrospun fibrous mats. a) Insoluble fraction, evaluated with a water/ethanol solution. b-c) FE-SEM images of the PEO-5EU (b) and PEO-5EUMA (c) fibrous scaffolds after solvent treatment.

Table 2
Mechanical properties (elastic modulus E and strain at break ε), water vapor transmission rate (WVTR) and water contact angle of the photo-crosslinked electrospun fibrous mats.

Sample	E (MPa)	ε (%)	WVTR (g/m^2/24 hr)	Water contact angle (°)
PEO	15.5 ± 1.7	8.8 ± 3.6	1025	11.7 ± 1.5
PEO-1EU	15.3 ± 2.1	7.6 ± 3.6	1022	11.9 ± 1.3
PEO-1EUMA	16.4 ± 2.9	9.6 ± 4.4	1011	10.7 ± 1.5
PEO-3EU	20.5 ± 3.2	7.4 ± 3.9	894	10.6 ± 1.7
PEO-3EUMA	25.6 ± 4.2	8.1 ± 4.8	974	9.9 ± 2.0
PEO-5EU	20.6 ± 4.2	7.5 ± 3.0	892	9.2 ± 1.8
PEO-5EUMA	27.7 ± 3.4	7.7 ± 4.1	981	9.4 ± 2.1

showed water contact angles below 12°, indicating high surface wettability. The incorporation of hydrophobic eugenol caused only a slight reduction in permeability, while further enhancing surface hydrophilicity. This is likely because the eugenol was embedded within the PEO matrix, where its aromatic (hydrophobic) rings were surrounded by the hydrophilic polymer, allowing hydroxyl groups (hydrophilic) to be exposed at the surface. These findings confirm that all the investigated nanofibrous materials remain hydrophilic, permeable, and breathable.

Based on the comprehensive characterization of the photo-cured electrospun scaffolds, and considering their intended use as wound healing patches, the two formulations containing the highest concentrations of active additive (i.e., PEO-5EU and PEO-5EUMA) were selected for further biological evaluation, alongside the neat photo-crosslinked PEO-based material (i.e., PEO) for comparison.

3.3. *Biological performance assessment of the nanofibrous scaffolds*

3.3.1. *Cytocompatibility*

Despite the well-established cytocompatibility of PEO, its supplementation with eugenol essential oil may significantly impact cell viability [71]. To evaluate the cytocompatibility of eugenol-doped PEO scaffolds, both direct and indirect cytocompatibility assays were conducted, with results summarized in Fig. 4.

As shown in Fig. 4a, the direct assay results indicate that neither PEO-5EU nor PEO-5EUMA significantly reduced the viability of HGF cells ($p > 0.05$). These findings are consistent with those of Tong et al. [72], who reported the safety of EU at concentrations up to 50 μM.

Interestingly, after 48 h, PEO-5EUMA induced a slight, though not statistically significant, increase in cell viability. This effect may be related to eugenol's ability to accelerate wound healing [72]; however, evidence for a *direct* pro-proliferative effect of eugenol on fibroblasts is limited and often contradictory. Eber et al. [73] observed that eugenol in periodontal dressings slowed the proliferation of HGF. Therefore, the modest increase in cellular metabolism observed here may more plausibly reflect the favorable microenvironment produced by the entire formulation of the eugenol-doped PEO patches rather than a direct stimulatory action of eugenol on fibroblast proliferation. SEM micrographs of the samples after the direct cytocompatibility test further confirm the cell-friendly behavior of the eugenol-doped scaffolds. As an example, Fig. 4c shows the micrograph of PEO-5EUMA, where cells appear well-spread and elongated, exhibiting multiple contact points with the eugenol-containing patches. Additional evidence of cytocompatibility is provided in Figure S3 (Supporting Information), which displays a dense layer of cells covering the entire PEO-5EU surface and thus actively producing extracellular matrix in direct contact with the patch. These observations are consistent with the findings reported by Khunkitti et al. [74].

The direct cytocompatibility evaluation was intentionally limited to short exposure times (24–48 h) to assess acute cellular responses and to exclude immediate material-related cytotoxic effects. Longer-term biological interactions were instead investigated through standardized indirect assays conducted in accordance with ISO 10,993–5 and ISO 10,993–12, which are particularly relevant for evaluating the cytotoxic potential of soluble species released from the scaffolds. These species may include not only eugenol, but also degradation byproducts of the polymeric network, residual photoinitiator fragments, short polymer chains, or microgel domains generated during the crosslinking process. This combined approach more closely reflects realistic application scenarios, in which cells are not necessarily in continuous direct contact with the material but may be influenced by diffusible substances in the surrounding microenvironment. The results of the indirect cytotoxicity test, summarized in Fig. 4b, show that the compounds released from both PEO-5EU and PEO-5EUMA did not significantly reduce cell viability. This finding is consistent with the results of the direct cytocompatibility tests. Furthermore, considering the insoluble fractions of PEO-5EU and PEO-5EUMA, which correspond to 96 % and 81 %,

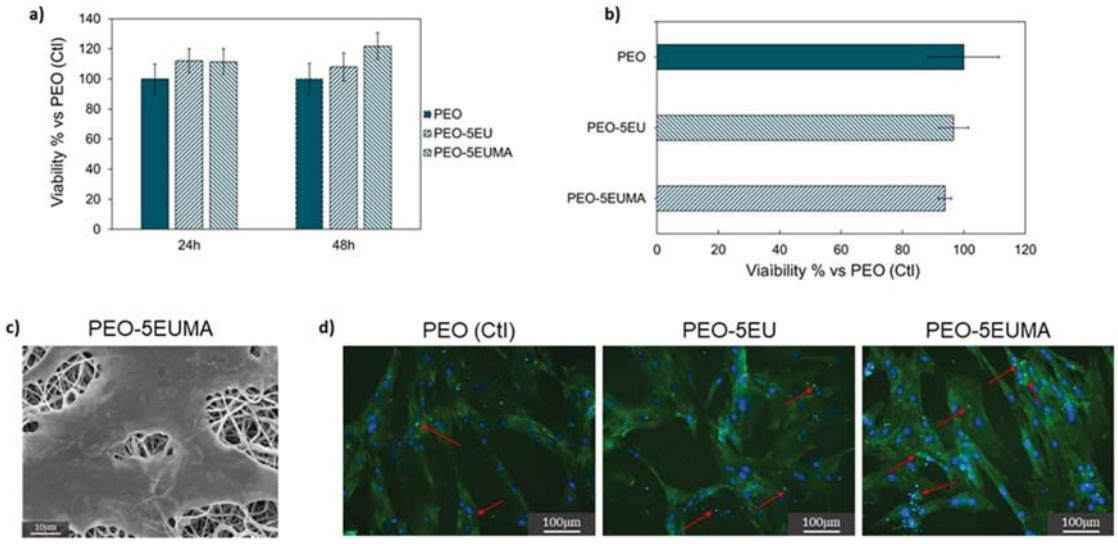

Fig. 4. Cytocompatibility results. a) Direct cytocompatibility results, assessed after 24 and 48 h of contact; b) indirect cytocompatibility results, performed in accordance with ISO 10,993–5; c) SEM micrograph showing cell distribution on PEO-5EUMA; d) morphological characterization of cells in contact with the eluate used for the indirect cytocompatibility test. Red arrows indicate scaffolds debris in proximity to the cells.

respectively (Fig. 3a), the concentration of eugenol released remains well below the cytotoxicity threshold. This finding is further supported by the fluorescent images in Fig. 4d, which depict normal cell morphology and distribution across all conditions, even in the presence of scaffold debris, as indicated by the red arrows in the figures.

3.3.2. Direct antibacterial activity

Given the significant impact of bacterial infections on the transition of acute wounds into chronic wounds, the antibacterial effects of eugenol-doped scaffolds have been evaluated against *Staphylococcus epidermidis* (a Gram-positive bacterium) and *E. coli*(a Gram-negative bacterium). Fig. 5a illustrates the differential effects of the eugenol additives contained in PEO scaffolds on Gram-positive and Gram-negative bacteria. PEO-5EU and PEO-5EUMA effectively reduce the viability of *S. epidermidis* compared to undoped PEO (** $p < 0.01$ and * $p < 0.05$, respectively), but do not significantly affect the viability of *E. coli* ($p > 0.05$). These results align with the study by Fajdek-Bieda et al. [75], which suggests that the difference in eugenol efficacy is likely due to structural variations in bacterial cell walls. Gram-positive bacteria possess a thicker peptidoglycan layer but lack an outer membrane, making them more susceptible to membrane-disrupting agents like polyphenols, including eugenol. In contrast, Gram-negative bacteria have an outer membrane rich in lipopolysaccharides, which can act as a barrier against antimicrobial compounds and contribute to resistance mechanisms [76]. However, this topic remains controversial, and the observed effect may be species-specific and strongly dose-dependent [77]. Furthermore, the analysis revealed a stronger antibacterial effect in scaffolds loaded with eugenol (PEO-5EU), which significantly reduced the viability of *S. epidermidis* compared to scaffolds loaded with the methacrylate form of eugenol (PEO-5EUMA, $ $p < 0.05$). This difference may be attributed to the inherent variations between the two incorporated active agents. The antimicrobial activity of eugenol primarily arises from its free phenolic hydroxyl group, which contributes to microbial inactivation through proton donation that disrupts cell membranes, hydrogen bonding with membrane proteins and lipids, and redox reactions that generate reactive oxygen species capable of damaging cellular components [78,79]. However, upon methacrylation, this phenolic hydroxyl group becomes esterified, thereby losing its ability to participate in these interactions and consequently diminishing the antimicrobial efficacy of the compound.

The CFU assay, presented in Fig. 5b, confirms the viability results, identifying PEO-5EU as the most effective material. However, since the colony count remained close to the initial infection level (10^3/well, indicated by the red line), these findings suggest a bacteriostatic rather than a bactericidal effect. This represents a novel finding compared to previous studies reported in the literature [59], but it can be explained by the multidrug-resistant nature of the bacterial strains, which alters the permeability of their cell membranes to antimicrobial agents [80]. The SEM micrographs of *S. epidermidis* shown in Fig. 5c are consistent with the results of the viability assay and bacterial count. In the PEO control, the scaffold is heavily colonized, with clusters and individual bacteria homogeneously distributed across the surface. In PEO-5EU, the

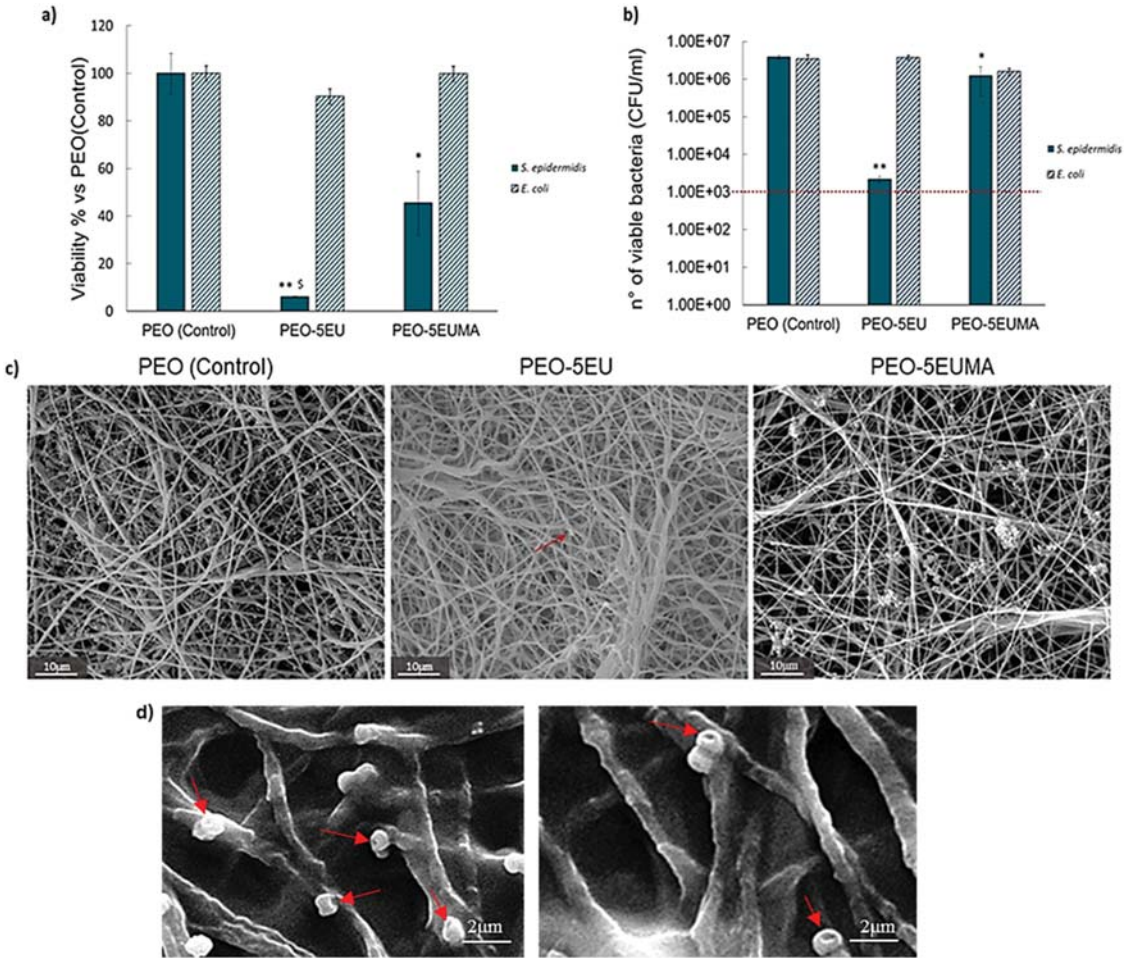

Fig. 5. Direct antibacterial activity. a) Percentage of *S. epidermidis* (light grey bar) and *E. coli*(dark grey bar) viability, estimated using metabolic activity; b) Number of viable bacteria, with the initial infection count indicated by the red line; c) SEM images of *Staphylococcus epidermidis* bacterial colonies on the scaffolds; and d) representative high-magnification SEM images showing membrane damage in *S. epidermidis* cells (pores indicated by red arrows). *, $ $p < 0.05$, ** $p < 0.01$.

surface appears nearly pristine, with very few detectable bacterial cells. In PEO-5EUMA, both bacteria-rich and bacteria-free areas are observed. Higher-magnification SEM images (Fig. 5d, representative for *S. epidermidis*) reveal the presence of pores and severe morphological alterations in the bacterial membranes of cells cultured on PEO-5EU scaffolds (highlighted by red arrows). These observations provide direct visual evidence supporting the hypothesis that the antibacterial activity arises from eugenol-induced disruption of bacterial membrane integrity, leading to irreversible membrane damage. Collectively, these findings support the effective bioavailability of eugenol-based compounds at the scaffold surface.

3.3.3. Indirect antibacterial activity

An indirect antibacterial assay was performed to assess the effect of soluble species released into conditioned media prepared in accordance with ISO 10,993–5 and ISO 10,993–12 on bacterial viability. Since the colonization of the wound area typically begins with Gram-positive species, the antibiofilm effect of the eugenol-doped materials was tested against *Staphylococcus epidermidis* as representative strain. The results, summarized in Fig. 6, confirm the higher efficacy of PEO doped with eugenol (PEO-5EU) compared to both the control (PEO) and the sample containing methacrylated eugenol (PEO-5EUMA). Specifically, PEO-5EU significantly reduces both bacterial metabolic activity (Fig. 6a, $p < 0.05$) and the number of bacterial colonies (Fig. 6b, $p < 0.05$). In contrast, PEO-5EUMA decreases the number of bacterial colonies but does not significantly affect bacterial metabolic activity. This result may be once again related to the nature and the chemical composition of the active agent used to dope the PEO polymer, as discussed in the previous section (i.e., the absence of the phenolic hydroxyl group in EUMA). However, regardless of the form, the eugenol released by the samples appears to inhibit biofilm formation (Fig. 6c). In the control sample (PEO), bacteria homogeneously cover the surface and begin to form a biofilm (red arrow). In contrast, bacteria exposed to the eluate collected from PEO-5EU and PEO-5EUMA remain as single cells and cover only a

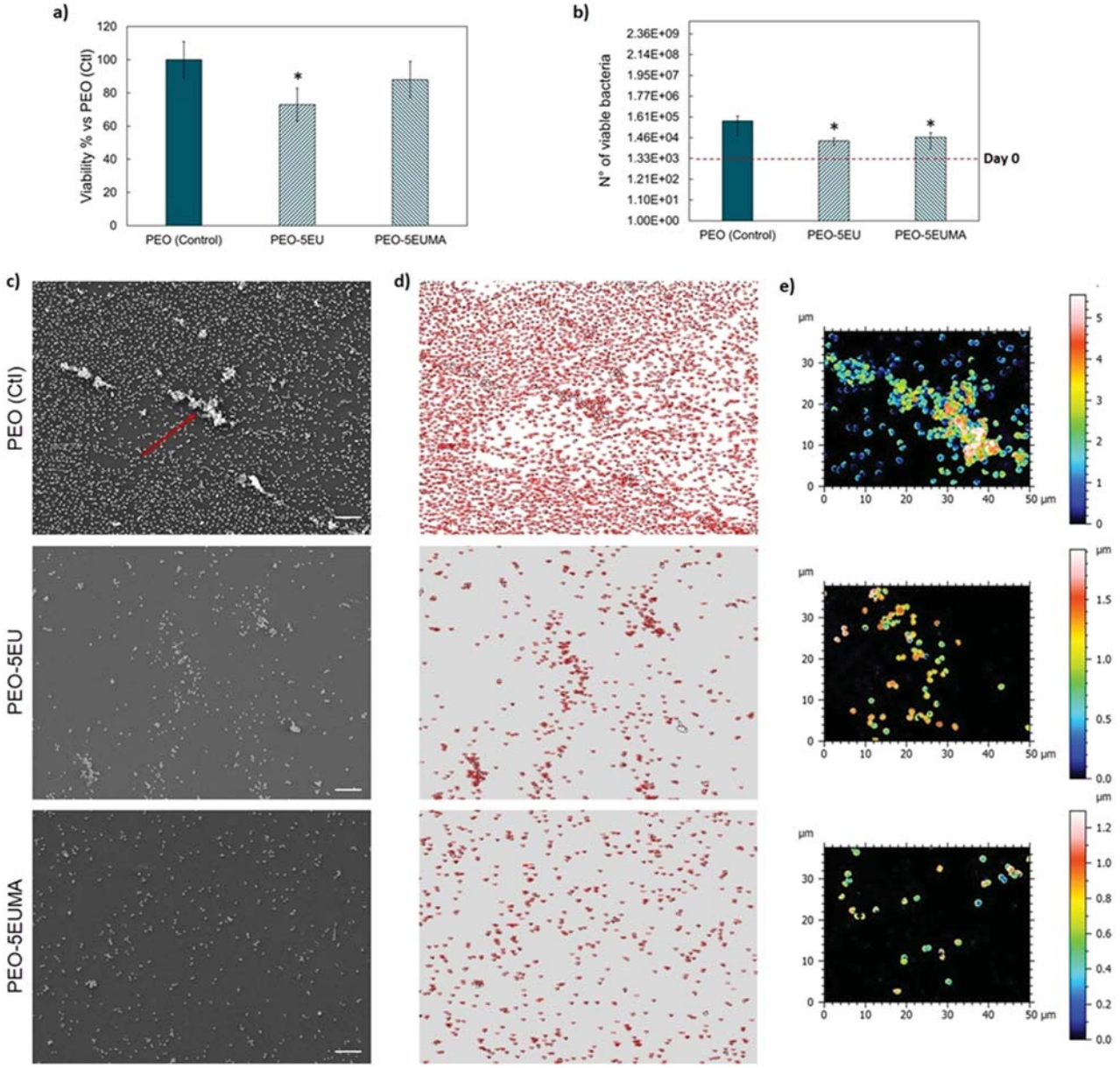

Fig. 6. Indirect antibacterial activity. a) Percentage of *S. epidermidis* (light grey bar) and *E. coli*(dark grey bar) metabolic activity; b) Number of viable bacteria, with the initial infection count indicated by the red line; c) SEM images showing the bacteria after the contact with the eluate collected from the samples; d) Area covered by the bacteria calculated by ImageJ. Scale bar = 10 µm. * $p < 0.05$.

limited area of the surface. SEM micrographs analyzed using ImageJ (Fig. 6d) estimate that the area covered by bacteria in the control (PEO) is 20.3 % ± 3.5 %, while in PEO-5EU and PEO-5EUMA, it is reduced to 2.2 % ± 0.6 % and 2.4 % ± 0.8 %, respectively. Moreover, the biofilm thickness analysis performed on SEM images using SmileView Map (Jeol) revealed a significant difference in biofilm thickness between bacteria in contact with the eluate collected from PEO (approximately 5 μm) and those exposed to the eluate from eugenol-doped PEO (both around 1 μm, corresponding to single colonies). These findings are supported by the research of Ribeiro et al. [81]: in their systematic review, authors demonstrated that eugenol can disrupt mature biofilms, reduce the genetic expression of virulence factors, prevent biofilm formation, and inhibit the bacterial quorum sensing.

3.3.4. Cells/bacteria co-culture

To simultaneously preserve cell viability and inhibit bacterial proliferation in the context of wound infections, the protective effect of eugenol-doped PEO-based scaffolds was evaluated using a cell/bacteria co-culture system. The results, summarized in Fig. 7, indicate that both PEO-5EU and PEO-5EUMA preserve cell numbers while significantly reducing bacterial load (* $p < 0.05$). Notably, PEO-5EUMA exhibits superior antibacterial efficacy compared to PEO-5EU, reducing the bacterial count to below the initial infection level. The minor discrepancy relative to the antibacterial results presented above likely arises from differences in the experimental methodologies employed in the two assays. SEM images presented in Fig. 7c show that both PEO-5EU and PEO-5EUMA supported cell adhesion and preserved a typical, healthy morphology, indicating favorable biocompatibility. In sharp contrast, no cells were detectable on the undoped PEO surface, highlighting the inability of the pristine material to sustain cell attachment. Although some bacterial aggregates were observed on the membranes of cells cultured on PEO-5EUMA, no detrimental effects on cell viability were detected. These findings demonstrate that the eugenol-doped PEO scaffolds not only promote cellular adhesion and proliferation but may also help preserve cell health even under bacterial challenge. Such behavior is likely attributable to the specific microenvironment generated by the surface characteristics of the doped materials, which could potentiate the intrinsic antimicrobial activity of human gingival fibroblasts [82].

3.4. Assessment of the pro-regenerative ability of the nanofibrous scaffolds

The regenerative potential of PEO-based nanofibrous materials incorporating eugenol, in its unmodified and methacrylated form, was assessed employing a scratch assay on human mesenchymal stromal cells (MSCs). MSCs have a key role in deep tissue regeneration because of their capacity to migrate to the site of injury, secrete trophic and immunomodulatory molecules [83]. The function of these cells facilitates the resolution of inflammation, angiogenesis, and the remodeling of the extracellular matrix, processes that are essential for the repair of the structural and functional integrity of damaged tissue.

Similar to the indirect cytocompatibility assay, the samples were immersed in serum-free cell culture medium and incubated at 37 °C with shaking at 120 rpm for one week. Fig. 8 presents the results obtained by acquiring images every hour over a 24-hour period, with three representative time points selected (0 h, 10 h, and 24 h; Fig. 8b). As shown in Fig. 8a, after 24 h, the PEO control, PEO-5EU, and PEO-5EUMA samples exhibited a significantly smaller scratch width (%) compared to the POLY sample, representing cells cultured on polystyrene multiwell plates without the addition of conditioned medium. Specifically, POLY induced only a 35 % wound width reduction, whereas PEO, PEO-5EU, and PEO-5EUMA induced reductions of 65 %, 67 %, and 85 %, respectively.

The comparable healing performance of the PEO and PEO-5EU eluates suggests that the incorporation of EU at this concentration does not significantly alter the material cytocompatibility, as already discussed above (Fig. 4). It is worth noting that residual benzophenone, used as a photoinitiator during scaffold preparation, may contribute to enhanced cell proliferation by promoting progression through the cell cycle [84]. Interestingly, the PEO-5EUMA scaffold showed the most pronounced wound closure effect, achieving an 80 % reduction in scratch width within 24 h, with approximately 50 % closure occurring between 6 and 10 h after exposure to the eluate. This enhanced cellular response could be attributed to the higher soluble fraction of the EUMA-containing sample (Fig. 3), which may facilitate a more sustained or controlled release of bioactive species, thereby supporting cell migration and proliferation.

Although the cytotoxicity of EU at high concentrations has been reported, recent studies indicate that, when properly delivered, this compound can exert beneficial effects on MSC behavior, enhancing cell

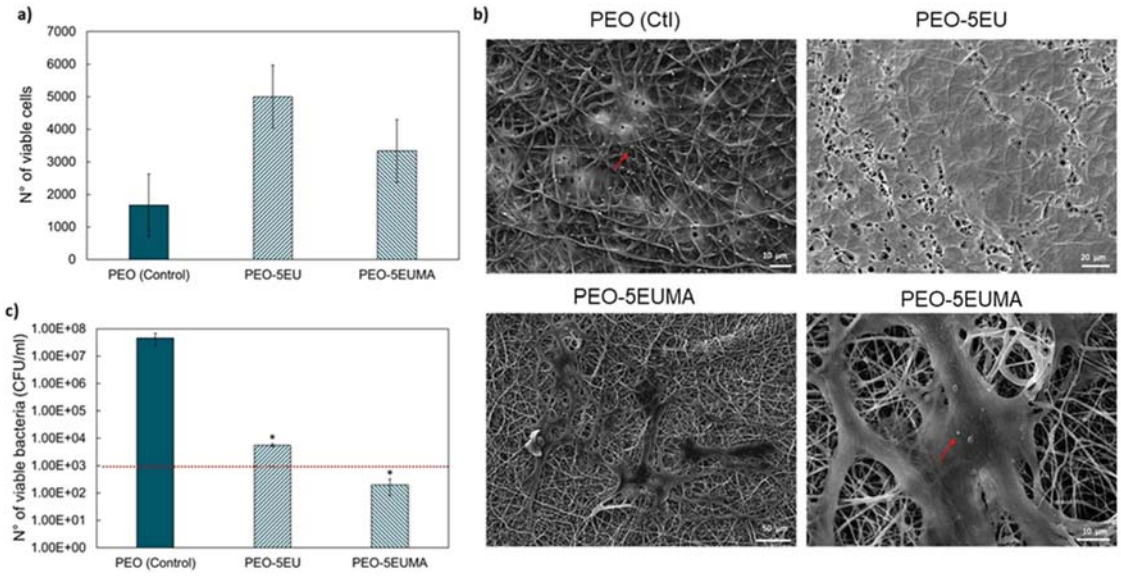

Fig. 7. Cells/bacteria co-culture system. a) Number of viable cells after 24 h; b) Number of viable bacteria (the initial bacterial load is indicated by the red line); c) SEM micrographs showing cell morphology. Scale bars = 10 μm and 50 μm. $p < 0.05$.

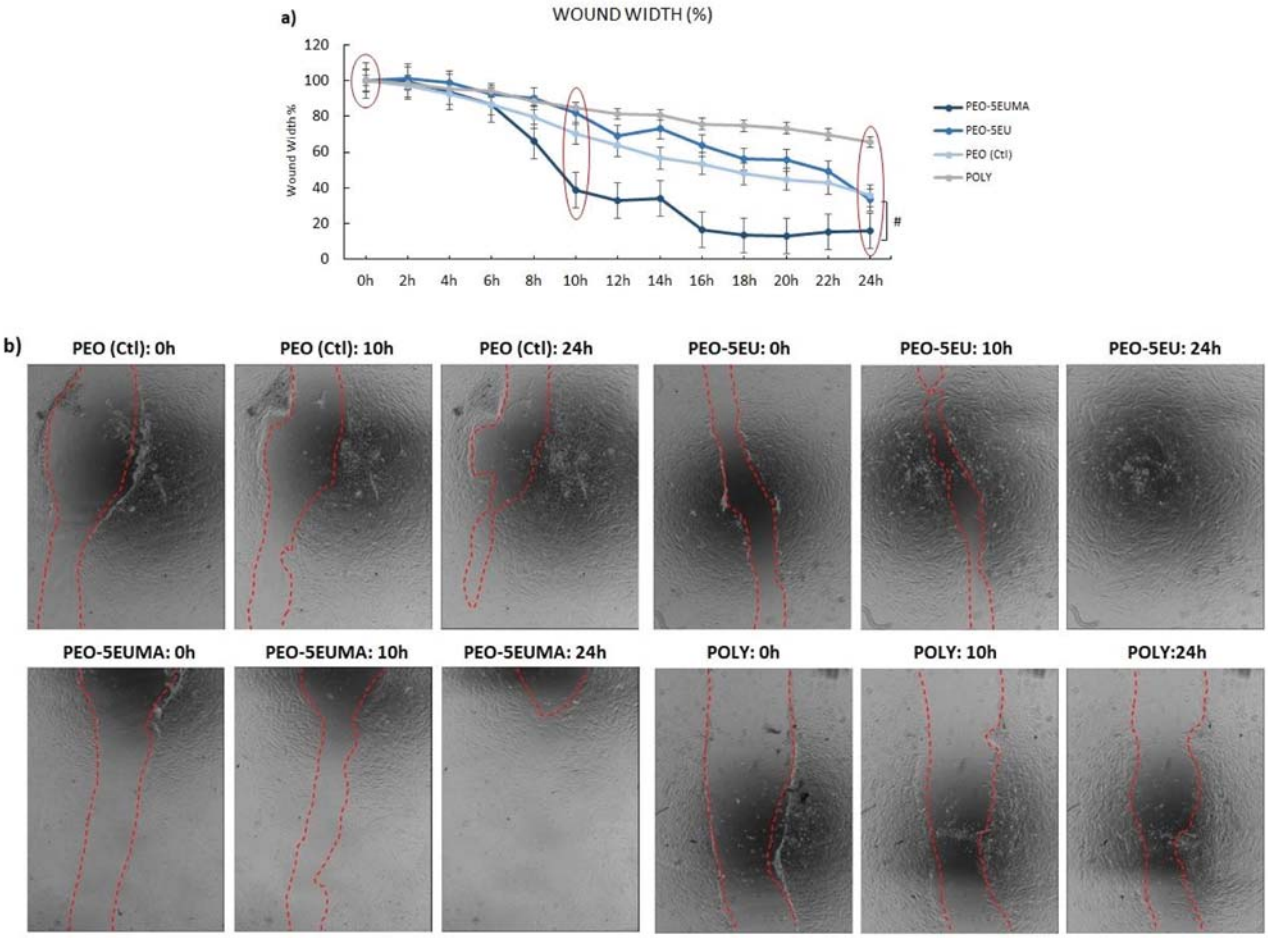

Fig. 8. 2D scratch test. a) Wound width reduction (%). Three time points (0, 10 h, 24 h) are highlighted by red circles; b) Representative images at 0, 10, and 24 h for PEO, PEO-5EU, PEO-5EUMA, and POLY.

survival, proliferation, and even lineage differentiation [85]. This renders it a suitable candidate for integration into smart wound dressings that will come in contact with either endogenous or exogenously applied MSCs, thereby enabling superficial and deep tissue regeneration.

Following monolayer tests, the pro-regenerative potential of the eugenol-doped patches was evaluated using a commercial

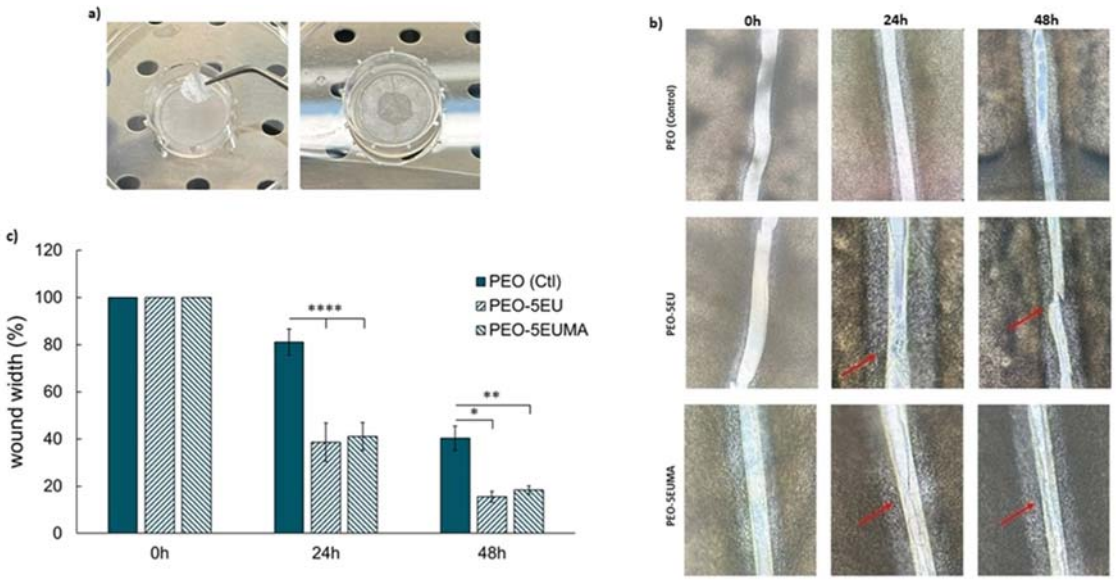

Fig. 9. 3D wound assay. a) PEO patch in contact with the wound on reconstructed human epidermis; b) Wound width (%) measured at 0, 24, and 48 h; c) Representative images of the wound used for the analysis. * $p < 0.05$; ** $p < 0.01$; **** $p < 0.0001$.

Reconstructed Human Epidermis (RhE) model. The RhE system replicates the three-dimensional architecture, barrier properties, and differentiation profile of native human skin, making it a biologically relevant platform for advanced in vitro assessments. In this environment, keratinocytes undergo stratification and maturation, forming a multilayered epidermis with distinct basal and cornified layers analogous to those of native tissue. The ability of RhE to maintain both structural complexity and functional differentiation is therefore crucial for studying epidermal responses and barrier-related phenomena at an advanced in vitro level, prior to progression toward appropriate in vivo animal models, where additional factors such as local and systemic inflammatory responses can be assessed [86].

For the tests, a wound was created using a scalpel, cutting through both the stratum corneum and basal layers. The patches were then applied and rinsed with a few microliters of culture medium (Fig. 9a) and maintained in an incubator for 48 h, with wound closure monitored at 24 and 48 h. The results are presented in Fig. 9.

Both eugenol-containing formulations exhibited significantly accelerated wound healing, achieving closure approximately twice as fast as undoped PEO. The difference in the "wound" width in the models in contact with PEO, PEO-5EU, and PEO-5EUMA is visible in Fig. 9b.

After 24 h (Fig. 9c), PEO-5EU and PEO-5EUMA induced wound closure of about 60 %, compared to 20 % with undoped PEO (**** $p < 0.0001$). After 48 h, the same trend was maintained, with both eugenol-doped PEO samples promoting approximately 80 % wound closure, versus 60 % for undoped PEO (** $p < 0.01$ vs. PEO-5EU; * $p < 0.05$ vs. PEO-5EUMA).

The differences observed between the 2D and 3D wound models (i.e., the more pronounced healing effect of PEO-5EUMA in the 2D assay versus the similar performance of PEO-5EU and PEO-5EUMA in the 3D model) can be attributed to the distinct analytical approaches. In the 2D assay, wound healing behavior is assessed based on the bioactivity of the sample eluate, reflecting the release of soluble compounds into the medium. In contrast, the 3D assay involves direct contact between the scaffold and the skin scratch, offering a more physiologically relevant setup that accounts for both material-cell interactions and degradation behavior. Consequently, the 3D model provides a more accurate representation of the overall wound healing potential of the developed scaffolds. These results are consistent with previous studies [87], which also reported enhanced wound healing in eugenol-functionalized nanofibrous systems. Such agreement further supports the beneficial role of eugenol in promoting tissue regeneration when properly incorporated into polymeric matrices.

4. Conclusions

In this study, poly(ethylene oxide) (PEO)-based electrospun membranes were functionalized with eugenol (EU) and eugenol methacrylate (EUMA) as bioactive agents for advanced wound-healing applications. Different active-agent concentrations were systematically investigated, while photo-crosslinking was employed to enhance stability and broaden biomedical applicability.

The resulting scaffolds consisted of uniform, defect-free fibers (316–340 nm in diameter) with an insoluble fraction above 81 % and an elastic modulus of 21–28 MPa, confirming robust mechanical properties. All scaffolds were flexible, hydrophilic, and permeable, meeting key requirements for wound dressing applications. Among the tested formulations, those containing the highest concentrations of active agents (PEO-5EU and PEO-5EUMA) exhibited the most promising performance and were therefore selected for biological evaluation.

Biological assessments demonstrated that both EU- and EUMA-functionalized scaffolds were cytocompatible and non-toxic, as confirmed by direct and indirect assays. The materials showed pronounced antibacterial activity against Gram-positive bacteria, with reduced efficacy against Gram-negative strains. Notably, PEO-5EU exhibited stronger antibacterial and anti-colonization effects, while both eugenol-doped scaffolds significantly reduced biofilm formation. In cell–bacteria co-culture assays, both membranes preserved cell viability under bacterial challenge, with PEO-5EUMA showing slightly greater cytoprotective effects.

The pro-regenerative potential of the scaffolds was demonstrated in both 2D and 3D wound-healing models. In the 2D monolayer assay, PEO-5EUMA promoted an 85 % reduction in wound width within 24 h. In the 3D reconstructed human epidermis model, both eugenol-doped scaffolds accelerated wound closure by approximately twofold relative to PEO, achieving ~60 % reduction after 24 h and ~80 % after 48 h. These results provide a highly encouraging preliminary indication of the regenerative potential of the developed materials and support further investigation in appropriate in vivo models.

Overall, this work introduces a novel and versatile strategy for the design of multifunctional wound dressings by integrating essential oil-derived compounds into photo-crosslinked electrospun PEO scaffolds. The direct comparison between eugenol and its methacrylated derivative elucidates how chemical modification and network architecture govern the balance between antimicrobial efficacy and regenerative performance. Collectively, these findings highlight the potential of eugenol-functionalized PEO nanofibrous membranes as a versatile and scalable platform for next-generation multifunctional wound dressings capable of simultaneously supporting infection control and tissue repair.

CRediT authorship contribution statement

A.C. Scalia: Writing – original draft, Visualization, Methodology, Investigation, Conceptualization. **J.A. Talamo Ruiz:** Writing – original draft, Visualization, Methodology, Investigation. **S. Dalle Vacche:** Writing – review & editing. **R. Bongiovanni:** Writing – review & editing, Resources. **P. Lacroix-Desmazes:** Writing – review & editing, Resources. **A. Cochis:** Writing – review & editing, Supervision, Resources, Conceptualization. **A. Vitale:** Writing – review & editing, Supervision, Resources, Methodology, Funding acquisition, Conceptualization.

Declaration of competing interest

The authors declare that they have no known competing financial interests or personal relationships that could have appeared to influence the work reported in this paper.

Acknowledgements

The authors thank Samantha Molina-Gutiérrez for the synthesis of methacrylic eugenol and Lucrezia Cianciaruso for her support with the biological evaluation of the samples.

Supplementary materials

Supplementary material associated with this article can be found, in the online version, at doi:10.1016/j.apmt.2026.103136.

Data availability

Data will be made available on request.

References

[1] C.K. Sen, Human wounds and its burden: an updated compendium of estimates, Adv. Wound Care 8 (2019) 39–48, https://doi.org/10.1089/wound.2019.0946.
[2] X. Ding, Q. Tang, Z. Xu, Y. Xu, H. Zhang, D. Zheng, S. Wang, Q. Tan, J. Maitz, P. K. Maitz, S. Yin, Y. Wang, J. Chen, Challenges and innovations in treating chronic and acute wound infections: from basic science to clinical practice, Burns. Trauma 10 (2022) tkac014, https://doi.org/10.1093/burnst/tkac014.
[3] X. Zhu, M.M. Olsson, R. Bajpai, K. Järbrink, W.E. Tang, J. Car, Health-related quality of life and chronic wound characteristics among patients with chronic wounds treated in primary care: a cross-sectional study in Singapore, Int. Wound J. 19 (2022) 1121–1132, https://doi.org/10.1111/iwj.13708.

[4] C.K. Sen, Human wound and its burden: updated 2020 compendium of estimates, Adv. Wound Care 10 (2021) 281–292, https://doi.org/10.1089/wound.2021.0026.

[5] I. Cavallo, F. Sivori, A. Mastrofrancesco, E. Abril, M. Pontone, E.G. Di Domenico, F. Pimpinelli, Bacterial biofilm in chronic wounds and possible therapeutic approaches, Biol. (Basel) 13 (2024) 109, https://doi.org/10.3390/biology13020109.

[6] M. Dinić, R. Verpile, J.L. Burgess, J. Ming, J. Marjanovic, C.N. Beliz, L. Plano, S. Hower, S.R. Thaller, S. Banerjee, H. Lev-Tov, M. Tomic-Canic, I. Pastar, Multi-drug resistant Staphylococcus epidermidis from chronic wounds impair healing in human wound model, WRR 32 (2024) 799–810, https://doi.org/10.1111/wrr.13231.

[7] X. Wang, H. Wang, J. Zhang, Y. Huang, Y. Wu, Y. Wang, R. Zhang, Morphological variability of *Escherichia coli* colonizing human wounds: a case report, BMC. Infect. Dis. 25 (2025) 440, https://doi.org/10.1186/s12879-025-10484-7.

[8] S. Guo, L.A. Dipietro, Factors affecting wound healing, J. Dent. Res. 89 (2010) 219–229, https://doi.org/10.1177/0022034509359125.

[9] N. Mahajan, S. Soker, S.V. Murphy, Regenerative medicine approaches for skin wound healing: from allografts to engineered skin substitutes, Curr. Transpl. Rep. 11 (2024) 207–221, https://doi.org/10.1007/s40472-024-00453-5.

[10] A. Alberts, D.-I. Tudorache, A.-G. Niculescu, A.M. Grumezescu, Advancements in wound dressing materials: highlighting recent progress in hydrogels, foams, and antimicrobial dressings, Gels. 11 (2025) 123, https://doi.org/10.3390/gels11020123.

[11] E. Rezvani Ghomi, M. Niazi, S. Ramakrishna, The evolution of wound dressings: from traditional to smart dressings, Polym. Adv. Technol. 34 (2023) 520–530, https://doi.org/10.1002/pat.5929.

[12] T. Lagoa, M.C. Queiroga, L. Martins, An overview of wound dressing materials, Pharmaceuticals 17 (2024) 1110, https://doi.org/10.3390/ph17091110.

[13] M. Sheikholeslam, M.E.E. Wright, M.G. Jeschke, S. Amini-Nik, Biomaterials for skin substitutes, Adv Heal. Mater. 7 (2018), https://doi.org/10.1002/adhm.201700897.

[14] A. Sood, M.S. Granick, N.L. Tomaselli, Wound dressings and comparative effectiveness data, Adv. Wound Care 3 (2014) 511–529, https://doi.org/10.1089/wound.2012.0401.

[15] B.S. Alotaibi, M. Khan, N.A. Ibrahim, A.K. Khan, R. Liaqat, M. Ijaz, Smart nanofibers in wound healing: exploring novel combinations and applications, CDD 22 (2025), https://doi.org/10.2174/0115672018376778250616113903.

[16] A. Sadeghi-avalshahr, S. Nazarnezhad, H. Hassanzadeh, M. Kazemi Noughabi, N. Namaei-Ghasemnia, M. Jalali, Synergistic effects of incorporated additives in multifunctional dressings for chronic wound healing: an updated comprehensive review, Wound Repair. Regen. 33 (2025) e13238, https://doi.org/10.1111/wrr.13238.

[17] Yixia Zhang, C. Xue, Yunpeng Zhang, Q. Zhang, K. Zhang, Y. Liu, Z. Shan, W. Qiu, G. Chen, N. Li, H. Zhang, J. Zhao, D.-P. Yang, Cocktail effect of ionic patch driven by triboelectric nanogenerator for diabetic wound healing, Chin. Chem. Lett. 35 (2024) 109196, https://doi.org/10.1016/j.cclet.2023.109196.

[18] H.M. Nguyen, T.T. Ngoc Le, A.T. Nguyen, H.N. Thien Le, T.T. Pham, Biomedical materials for wound dressing: recent advances and applications, RSC Adv. 13 (2023) 5509–5528, https://doi.org/10.1039/D2RA07673J.

[19] F.V. Borbolla-Jiménez, S.I. Peña-Corona, S.J. Farah, M.T. Jiménez-Valdés, E. Pineda-Pérez, A. Romero-Montero, M.L. Del Prado-Audelo, S.A. Bernal-Chávez, J.J. Magaña, G. Leyva-Gómez, Films for wound healing fabricated using a solvent casting technique, Pharmaceutics 15 (2023) 1914, https://doi.org/10.3390/pharmaceutics15071914.

[20] S. Alven, S. Peter, Z. Mbese, B.A. Aderibigbe, Polymer-based wound dressing materials loaded with bioactive agents: potential materials for the treatment of diabetic wounds, Polym. (Basel) 14 (2022) 724, https://doi.org/10.3390/polym14040724.

[21] C. Du, J. Liu, D.A. Fikhman, K.S. Dong, M.B.B. Monroe, Shape memory polymer foams with phenolic acid-based antioxidant and antimicrobial properties for traumatic wound healing, Front. Bioeng. Biotechnol. 10 (2022) 809361, https://doi.org/10.3389/fbioe.2022.809361.

[22] A. Hargis, M. Yaghi, N.M. Bermudez, A. Gefen, Foam dressings for wound healing, Curr. Derm. Rep. 13 (2024) 28–35, https://doi.org/10.1007/s13671-024-00422-2.

[23] Q. Li, X. Lai, Y. Duan, F. Jiang, Y. Li, Z. Huang, S. Liu, Y. Wang, C. Jiang, C. Zhang, X. Pan, 3D nanofiber sponge based on natural insect quaternized chitosan/pullulan/citric acid for accelerating wound healing, Carbohydr. Polym. 348 (2025) 122827, https://doi.org/10.1016/j.carbpol.2024.122827.

[24] Y. Fang, Y. Xu, Z. Wang, W. Zhou, L. Yan, X. Fan, H. Liu, 3D porous chitin sponge with high absorbency, rapid shape recovery, and excellent antibacterial activities for noncompressible wound, Chem. Eng. J. 388 (2020) 124169, https://doi.org/10.1016/j.cej.2020.124169.

[25] Z. Shen, C. Zhang, T. Wang, J. Xu, Advances in functional hydrogel wound dressings: a review, Polym. (Basel) 15 (2023) 2000, https://doi.org/10.3390/polym15092000.

[26] Y. Liang, J. He, B. Guo, Functional hydrogels as wound dressing to enhance wound healing, ACS Nano 15 (2021) 12687–12722, https://doi.org/10.1021/acsnano.1c04206.

[27] Y. Cho, J.W. Baek, M. Sagong, S. Ahn, J.S. Nam, I. Kim, Electrospinning and nanofiber technology: fundamentals, innovations, and applications, Adv. Mater. 37 (2025) 2500162, https://doi.org/10.1002/adma.202500162.

[28] D. Ji, Y. Lin, X. Guo, B. Ramasubramanian, R. Wang, N. Radacsi, R. Jose, X. Qin, S. Ramakrishna, Electrospinning of nanofibres, Nat. Rev. Methods Primers. 4 (2024) 1, https://doi.org/10.1038/s43586-023-00278-z.

[29] S. Zhang, W. Yang, W. Gong, Y. Lu, D.-G. Yu, P. Liu, Recent progress of electrospun nanofibers as burning dressings, RSC. Adv. 14 (2024) 14374–14391, https://doi.org/10.1039/D4RA01514B.

[30] R.S. Ambekar, B. Kandasubramanian, Advancements in nanofibers for wound dressing: a review, Eur. Polym. J. 117 (2019) 304–336, https://doi.org/10.1016/j.eurpolymj.2019.05.020.

[31] X. Zhang, Y. Wang, Z. Gao, X. Mao, J. Cheng, L. Huang, J. Tang, Advances in wound dressing based on electrospinning nanofibers, J Appl. Polym. Sci. 141 (2024) e54746, https://doi.org/10.1002/app.54746.

[32] F. Jonidi Shariatzadeh, S. Currie, S. Logsetty, R. Spiwak, S. Liu, Enhancing wound healing and minimizing scarring: a comprehensive review of nanofiber technology in wound dressings, Prog. Mater. Sci. 147 (2025) 101350, https://doi.org/10.1016/j.pmatsci.2024.101350.

[33] A. Partovi, M. Khedrinia, S. Arjmand, S.O. Ranaei Siadat, Electrospun nanofibrous wound dressings with enhanced efficiency through carbon quantum dots and citrate incorporation, Sci. Rep. 14 (2024) 19256, https://doi.org/10.1038/s41598-024-70295-9.

[34] X. Chen, Y. Chen, B. Fu, K. Li, D. Huang, C. Zheng, M. Liu, D.-P. Yang, Eggshell membrane-mimicking multifunctional nanofiber for in-situ skin wound healing, Int. J. Biol. Macromol. 210 (2022) 139–151, https://doi.org/10.1016/j.ijbiomac.2022.04.212.

[35] L. Zheng, Z. Zhu, L. Pan, L. Zhong, S. Xiao, C. Zhao, Y. Liu, J. Xu, Y. Zhang, Polysaccharides and proteins as natural polymers for electrospun wound dressings: a review of healing potential, challenges, and crosslinking strategies, Int. J. Biol. Macromol. 320 (2025) 145960, https://doi.org/10.1016/j.ijbiomac.2025.145960.

[36] J. Kou, Y. Li, C. Zhou, X. Wang, J. Ni, Y. Lin, H. Ge, D. Zheng, G. Chen, X. Sun, Q. Tan, Electrospinning in promoting chronic wound healing: materials, process, and applications, Front. Bioeng. Biotechnol. 13 (2025) 1550553, https://doi.org/10.3389/fbioe.2025.1550553.

[37] K. Chen, H. Hu, Y. Zeng, H. Pan, S. Wang, Y. Zhang, L. Shi, G. Tan, W. Pan, H. Liu, Recent advances in electrospun nanofibers for wound dressing, Eur. Polym. J. 178 (2022) 111490, https://doi.org/10.1016/j.eurpolymj.2022.111490.

[38] N. Yuan, K. Shao, S. Huang, C. Chen, Chitosan, alginate, hyaluronic acid and other novel multifunctional hydrogel dressings for wound healing: a review, Int. J. Biol. Macromol. 240 (2023) 124321, https://doi.org/10.1016/j.ijbiomac.2023.124321.

[39] A.D. Juncos Bombin, N.J. Dunne, H.O. McCarthy, Electrospinning of natural polymers for the production of nanofibres for wound healing applications, Mater. Sci. Eng.: C 114 (2020) 110994, https://doi.org/10.1016/j.msec.2020.110994.

[40] S. Kwon, S. Shim, K.-H. Yu, M. Seong, D. Lee, Advances in electrospun nanofibers for Biomed, Eng. Fibers Polym. (2025), https://doi.org/10.1007/s12221-025-01219-1.

[41] Q. Wang, P. Ji, T. Bu, Y. Mao, H. He, N. Ge, Recent progress in the application of electrospinning technology in the biomedical field, JFB 16 (2025) 266, https://doi.org/10.3390/jfb16070266.

[42] M.A. Mohammadi, A.M. Alizadeh, M. Mousavi, F. Hashempour-baltork, S. Kooki, M.R. Shadan, S.M. Hosseini, D.J. McClements, Advances and applications of crosslinked electrospun biomacromolecular nanofibers, Int. J. Biol. Macromol 271 (2024) 132743, https://doi.org/10.1016/j.ijbiomac.2024.132743.

[43] P. Kianfar, S. Dalle Vacche, G. Fredi, R. Bongiovanni, A. Vitale, Photo-induced processes for the fabrication of nanocomposite PEO/GO electrospun nanofibers with enhanced thermal conductivity, Monatsh. Chem. (2025), https://doi.org/10.1007/s00706-025-03374-w.

[44] P. Kianfar, A. Vitale, S. Dalle Vacche, R. Bongiovanni, Enhancing properties and water resistance of PEO-based electrospun nanofibrous membranes by photo-crosslinking, J. Mater. Sci. 56 (2021) 1879–1896, https://doi.org/10.1007/s10853-020-05346-3.

[45] G. Fredi, P. Kianfar, S. Dalle Vacche, A. Pegoretti, A. Vitale, Electrospun shape-stabilized phase change materials based on photo-crosslinked polyethylene oxide, Polym. (Basel) 13 (2021) 2979, https://doi.org/10.3390/polym13172979.

[46] P. Kianfar, S. Dalle Vacche, R. Bongiovanni, C. Mollea, F. Bosco, Z. Najmi, A. C. Scalia, A. Cochis, A. Vitale, Combining electrospinning and photoinduced reactions to fabricate cytocompatible and antibacterial Ag nanoparticle-decorated polymeric membranes, ACS Appl. Polym. Mater. 6 (2024) 14749–14759, https://doi.org/10.1021/acsapm.4c02953.

[47] A. Abdou, A. Elmakssoudi, A. El Amrani, J. JamalEddine, M. Dakir, Recent advances in chemical reactivity and biological activities of eugenol derivatives, Med. Chem. Res. 30 (2021) 1011–1030, https://doi.org/10.1007/s00044-021-02712-x.

[48] J. Kerosenewala, P. Vaidya, V. Ozarkar, Y. Shirapure, A.P. More, Eugenol: extraction, properties and its applications on incorporation with polymers and resins—A review, Polym. Bull. 80 (2023) 7047–7099, https://doi.org/10.1007/s00289-022-04414-9.

[49] A.A. Khalil, U.U. Rahman, M.R. Khan, A. Sahar, T. Mehmood, M. Khan, Essential oil eugenol: sources, extraction techniques and nutraceutical perspectives, RSC Adv. 7 (2017) 32669–32681, https://doi.org/10.1039/C7RA04803C.

[50] R.A. Bisergaeva, M.A. Takaeva, Y.N. Sirieva, Extraction of eugenol, a natural product, and the preparation of eugenol benzoate, J. Phys.: Conf. Ser 1889 (2021) 022085, https://doi.org/10.1088/1742-6596/1889/2/022085.

[51] N.S. Tripathy, L. Sahoo, S.K. Paikray, F. Dilnawaz, Eugenol: the phytocompound's potential biological applications, BioNanoSci 14 (2024) 4044–4055, https://doi.org/10.1007/s12668-024-01568-w.

[52] M.F. Nisar, M. Khadim, M. Rafiq, J. Chen, Y. Yang, C.C. Wan, Pharmacological properties and health benefits of Eugenol: a comprehensive review, Oxid. Med. Cell. Longev 2021 (2021) 2497354, https://doi.org/10.1155/2021/2497354.

[53] K. Pramod, S.H. Ansari, J. Ali, Eugenol: a natural compound with versatile pharmacological actions, Nat. Prod. Commun 5 (2010), https://doi.org/10.1177/1934578×1000501236, 1934578×1000501236.
[54] M. Ulanowska, B. Olas, Biological properties and prospects for the application of eugenol—A review, Int. J. Mol. Sci. 22 (2021) 3671, https://doi.org/10.3390/ijms22073671.
[55] A. Kowalewska, K. Majewska-Smolarek, Eugenol-based polymeric materials—Antibacterial activity and applications, Antibiotics 12 (2023) 1570, https://doi.org/10.3390/antibiotics12111570.
[56] Y. Wang, Y. Xue, Q. Bi, D. Qin, Q. Du, P. Jin, Enhanced antibacterial activity of eugenol-entrapped casein nanoparticles amended with lysozyme against gram-positive pathogens, Food Chem. 360 (2021) 130036, https://doi.org/10.1016/j.foodchem.2021.130036.
[57] M.K. Yadav, S. Park, S. Chae, J. Song, H.C. Kim, Antimicrobial activities of eugenia caryophyllata extract and its major chemical constituent eugenol against Streptococcus pneumoniae, APMIS 121 (2013) 1198–1206, https://doi.org/10.1111/apm.12067.
[58] S. Hemaiswarya, M. Doble, Synergistic interaction of eugenol with antibiotics against gram negative bacteria, Phytomedicine 16 (2009) 997–1005, https://doi.org/10.1016/j.phymed.2009.04.006.
[59] G.E. Jeyakumar, R. Lawrence, Mechanisms of bactericidal action of Eugenol against *Escherichia coli*, J. Herb. Med. 26 (2021) 100406, https://doi.org/10.1016/j.hermed.2020.100406.
[60] H. Moussa, B. El Omari, H. Chefchaou, M. Tanghort, A. Mzabi, N. Chami, A. Remmal, Action of thymol, carvacrol and eugenol on Penicillium and Geotrichum isolates resistant to commercial fungicides and causing postharvest citrus decay, Can. J. Plant Pathol 43 (2021) 26–34, https://doi.org/10.1080/07060661.2020.1767692.
[61] A.F. Olea, A. Bravo, R. Martínez, M. Thomas, C. Sedan, L. Espinoza, E. Zambrano, D. Carvajal, E. Silva-Moreno, H. Carrasco, Antifungal activity of eugenol derivatives against botrytis Cinerea, Molecules 24 (2019) 1239, https://doi.org/10.3390/molecules24071239.
[62] J. Bai, J. Li, Z. Chen, X. Bai, Z. Yang, Z. Wang, Y. Yang, Antibacterial activity and mechanism of clove essential oil against foodborne pathogens, LWT 173 (2023) 114249, https://doi.org/10.1016/j.lwt.2022.114249.
[63] S. Molina-Gutiérrez, A. Manseri, V. Ladmiral, R. Bongiovanni, S. Caillol, P. Lacroix-Desmazes, Eugenol: a promising building block for synthesis of radically polymerizable monomers, Macromol. Chem. Phys. 220 (2019) 1900179, https://doi.org/10.1002/macp.201900179.
[64] S. Molina-Gutiérrez, S. Dalle Vacche, A. Vitale, V. Ladmiral, S. Caillol, R. Bongiovanni, P. Lacroix-Desmazes, Photoinduced polymerization of eugenol-derived methacrylates, Molecules 25 (2020) 3444, https://doi.org/10.3390/molecules25153444.
[65] M.J.G. Fernandes, R.B. Pereira, D.M. Pereira, A.G. Fortes, E.M.S. Castanheira, M.S. T. Gonçalves, New eugenol derivatives with enhanced insecticidal activity, Int. J. Mol. Sci. 21 (2020) 9257, https://doi.org/10.3390/ijms21239257.
[66] F.F.M. Da Silva, F.J.Q. Monte, T.L.G. De Lemos, P.G.G. Do Nascimento, A.K. De Medeiros Costa, L.M.M. De Paiva, Eugenol derivatives: synthesis, characterization, and evaluation of antibacterial and antioxidant activities, Chem. Cent. J. 12 (2018) 34, https://doi.org/10.1186/s13065-018-0407-4.
[67] A.S.T.M. International, *Standard test methods for gravimetric determination of water vapor transmission rate of materials*, ASTM E96/E96M-24a, 2024.
[68] E. Rigo, C. Totée, V. Ladmiral, S. Caillol, P. Lacroix-Desmazes, 4-Vinyl guaiacol: a key intermediate for biobased polymers, Molecules 29 (2024) 2507, https://doi.org/10.3390/molecules29112507.
[69] X. Wang, B. Ding, G. Sun, M. Wang, J. Yu, Electro-spinning/netting: a strategy for the fabrication of three-dimensional polymer nano-fiber/nets, Prog. Mater. Sci. 58 (2013) 1173–1243, https://doi.org/10.1016/j.pmatsci.2013.05.001.
[70] J. Gutierrez-Gonzalez, E. Garcia-Cela, N. Magan, S.S. Rahatekar, Electrospinning alginate/polyethylene oxide and curcumin composite nanofibers, Mater. Lett. 270 (2020) 127662, https://doi.org/10.1016/j.matlet.2020.127662.
[71] V.T. Alexa, A. Galuscan, C.M. Soica, A. Cozma, D. Coricovac, F. Borcan, I. Popescu, A. Mioc, C. Szuhanek, C.A. Dehelean, D. Jumanca, Vitro assessment of the cytotoxic and antiproliferative profile of natural preparations containing bergamot, orange and clove essential oils, Molecules. 27 (2022) 990, https://doi.org/10.3390/molecules27030990.
[72] T. Tong, R. Geng, S.-G. Kang, X. Li, K. Huang, Revitalizing photoaging skin through eugenol in UVB-exposed hairless mice: mechanistic insights from integrated Multi-omics, Antioxidants 13 (2024) 168, https://doi.org/10.3390/antiox13020168.
[73] R.M. Eber, C.F. Shuler, W. Buchanan, F.M. Beck, J.E. Horton, Effect of periodontal dressings on Human gingival fibroblasts In vitro, J. Periodontol. 60 (1989) 429–434, https://doi.org/10.1902/jop.1989.60.8.429.
[74] W. Khunkitti, P. Veerapan, C. Hahnvajanawong, In vitro bioactivities of clove buds oil (Eugenia caryophyllata) and its effect on dermal fibroblast, Int. J. Pharm. Pharm. Sci. 4 (2012) 556–560.
[75] A. Fajdek-Bieda, J. Pawlińska, A. Wróblewska, W. Żwierełło, A. Łuś, A. Klimowicz, Antibacterial and preservative potential of eugenol and isoeugenol in cosmetics: a natural solution for product stability, Appl. Sci. 15 (2025) 2129, https://doi.org/10.3390/app15042129.
[76] K.P. Romano, D.T. Hung, Targeting LPS biosynthesis and transport in gram-negative bacteria in the era of multi-drug resistance, Biochim. Biophys. Acta (BBA) - Mol. Cell Res. 1870 (2023) 119407, https://doi.org/10.1016/j.bbamcr.2022.119407.
[77] H. Jafri, G. Banerjee, M.S.A. Khan, I. Ahmad, H.H. Abulreesh, A.S. Althubiani, Synergistic interaction of eugenol and antimicrobial drugs in eradication of single and mixed biofilms of Candida albicans and Streptococcus mutans, AMB Expr. 10 (2020) 185, https://doi.org/10.1186/s13568-020-01123-2.
[78] N. Ferrando, M.R. Pino-Otín, E. Terrado, D. Ballestero, E. Langa, Bioactivity of eugenol: a potential antibiotic adjuvant with minimal ecotoxicological impact, IJMS 25 (2024) 7069, https://doi.org/10.3390/ijms25137069.
[79] V. Khwaza, B.A. Aderibigbe, Antibacterial activity of selected essential oil components and their derivatives: a review, Antibiotics 14 (2025) 68, https://doi.org/10.3390/antibiotics14010068.
[80] K.E. Vivekanandan, P.V. Kumar, R.C. Jaysree, T. Rajeshwari, Exploring molecular mechanisms of drug resistance in bacteria and progressions in CRISPR/Cas9-based genome expurgation solutions, Glob. Med. Genet. 12 (2025) 100042, https://doi.org/10.1016/j.gmg.2025.100042.
[81] T.A.N. Ribeiro, G.A. Dos Santos, C.T. Dos Santos, D.C.F. Soares, M.F. Saraiva, D.H. S. Leal, D. Sachs, Eugenol as a promising antibiofilm and anti-quorum sensing agent: a systematic review, Microb. Pathog. 196 (2024) 106937, https://doi.org/10.1016/j.micpath.2024.106937.
[82] M. Lappin, M. Dellett, K. Mills, F. Lundy, C. Irwin, The neutralising and stimulatory effects of antimicrobial peptide LL-37 in human gingival fibroblasts, Arch. Oral Biol. 148 (2023) 105634, https://doi.org/10.1016/j.archoralbio.2023.105634.
[83] S. Balaji, S.G. Keswani, T.M. Crombleholme, The role of mesenchymal stem cells in the regenerative wound healing phenotype, Adv. Wound Care 1 (2012) 159–165, https://doi.org/10.1089/wound.2012.0361.
[84] M.-A. Park, K.-A. Hwang, H.-R. Lee, B.-R. Yi, E.-B. Jeung, K.-C. Choi, Benzophenone-1 stimulated the growth of BG-1 ovarian cancer cells by cell cycle regulation via an estrogen receptor alpha-mediated signaling pathway in cellular and xenograft mouse models, Toxicology 305 (2013) 41–48, https://doi.org/10.1016/j.tox.2012.12.021.
[85] S. Sisakhtnezhad, M. Heidari, A. Bidmeshkipour, Eugenol enhances proliferation and migration of mouse bone marrow-derived mesenchymal stem cells in vitro, Env. Toxicol. Pharmacol. 57 (2018) 166–174, https://doi.org/10.1016/j.etap.2017.12.012.
[86] J. Bajsert, V. De Glas, E. Faway, C. Lambert De Rouvroit, M. Pérez-Aso, P.W. Cook, Y. Poumay, Characterization of reconstructed Human epidermis in a chemically-defined, Anim. Orig.-Free Cell Cult. JID Innov. 4 (2024) 100298, https://doi.org/10.1016/j.xjidi.2024.100298.
[87] F. Noori, M. Osanloo, H.R. Moradi, H. Ghaderi Jafarbeigloo, M. Jirehnezhadyan, S. A. Kouhpayeh, M. Tirgare, A. Bozorgi, A. Goodarzi, Fabrication, characterization, and in vivo implantation of eugenol-loaded nanogels and PCL/Cs electrospun nanofibers for wound healing applications, J. Bioact. Compat. Polym. 38 (2023) 480–492, https://doi.org/10.1177/08839115231207337.